

Constraints on galactic outflows from the metallicity-stellar mass-SFR relation of EAGLE simulation and SDSS galaxies

Yuanye Lin¹ and Ying Zu^{1,2,3}*

¹Department of Astronomy, School of Physics and Astronomy, Shanghai Jiao Tong University, Shanghai 200240, China

²Shanghai Key Laboratory for Particle Physics and Cosmology, Shanghai Jiao Tong University, Shanghai 200240, China

³Key Laboratory for Particle Physics, Astrophysics and Cosmology, Ministry of Education, Shanghai Jiao Tong University, Shanghai 200240, China

Accepted XXX. Received YYY; in original form ZZZ

ABSTRACT

Stellar feedback-driven outflows regulate the stellar formation and chemical enrichment of galaxies, yet the underlying dependence of mass outflow rate on galaxy properties remains largely unknown. We develop a simple yet comprehensive non-equilibrium chemical evolution model (NE-CEM) to constrain the mass-loading factor η of outflows using the metallicity-stellar mass-SFR relation observed by SDSS at $z=0$. Our NE-CEM predicts the chemical enrichment by explicitly tracking both the histories of star formation and mass-loading. After exploring the EAGLE simulation, we discover a compact yet flexible model that accurately describes the average star formation histories of galaxies. Applying a novel method of chemically measuring η to EAGLE, we find η can be parametrised by its dependence on stellar mass and specific SFR as $\log \eta \propto M_*^\alpha s\text{SFR}^\beta$, with $\alpha=-0.12$ and $\beta=0.32$ in EAGLE. Our chemically-inferred η agrees remarkably well with the kinematic measurements by Mitchell et al. After extensive tests with EAGLE, we apply an NE-CEM Bayesian analysis to the SDSS data, yielding a tight constraint of $\log(\eta/0.631) = 0.731 \pm 0.002 \times (M_*/10^{9.5} M_\odot)^{-0.222 \pm 0.004} (s\text{SFR}/10^{-9.5} \text{yr}^{-1})^{0.078 \pm 0.003}$, in good agreement with the down-the-barrel measurements. Our best-fitting NE-CEM not only accurately describes the metallicity-stellar mass-SFR relation at $z=0$, but also successfully reproduce the so-called “fundamental metallicity relation” at higher redshifts. Our results reveal that different galaxies form stars and enrich their gas in a non-equilibrium but strikingly coherent fashion across cosmic time.

Key words: ISM: abundances — ISM: jets and outflows — galaxies: abundances — galaxies: evolution — galaxies: fundamental parameters — galaxies: ISM

1 INTRODUCTION

The metallicity of the interstellar medium (ISM) provides a key diagnostic of the ejective feedback mechanisms, i.e., galactic outflows (Heckman et al. 1990; Veilleux et al. 2005), in theories of galaxy formation (Somerville & Davé 2015; Naab & Ostriker 2017). In particular, the chemical enrichment history (CEH) of a galaxy is shaped by the interplay between metal production by stellar nucleosynthesis along the star formation history, metal dilution in the ISM by the accretion of metal-poor gas, and metal loss due to the ejection of metal-enriched material by outflows (Larson 1972; Tinsley 1980; Dekel & Silk 1986; Mac Low & Ferrara 1999; Dalcanton 2007; Finlator & Davé 2008; Andrews et al. 2017; Weinberg et al. 2017). In this paper, by examining such complex interplay in the EAGLE hydrodynamical simulation (Schaye et al. 2015; Crain et al. 2015), we develop a simple yet comprehensive chemical evolution model (CEM) to simultaneously reconstruct the average SFH and constrain the physics of galactic winds driven by stellar feedbacks, from the present-day metallicity (Z_{gas}), stellar mass (M_*), and star formation rate (SFR; \dot{M}_*) of galaxies observed by the Sloan Digital Sky Survey (SDSS; York et al. 2000).

One of the primary goals of galaxy CEMs in the literature is to provide an analytic framework for interpreting the observed scaling relations between the gaseous metallicity Z_{gas} (as measured by $\log \text{O}/\text{H}$, the oxygen-to-hydrogen abundance ratio in the ISM) and other physical properties of galaxies, as well as the redshift evolution (or lack thereof) of these relations (Maiolino & Mannucci 2019, and references therein). For instance, the positive correlation between oxygen abundance and stellar mass of galaxies (a.k.a., the mass-metallicity relation; MZR) has been observed in both the local Universe (Lequeux et al. 1979; Tremonti et al. 2004; Zahid et al. 2011; Andrews & Martini 2013; Gao et al. 2018; Huang et al. 2019) and at higher redshifts of $z \sim 1-3$ (Savaglio et al. 2005; Erb et al. 2006; Maiolino et al. 2008; Mannucci et al. 2009; Henry et al. 2013; Sanders et al. 2021; Wang et al. 2022b; Li et al. 2022). The MZR is likely driven by the anti-correlation between M_* and the mass-loading of outflows η , defined as

$$\eta = \frac{\text{mass outflow rate}}{\text{star formation rate}} = \frac{\dot{M}_{\text{out}}}{\dot{M}_*}, \quad (1)$$

because the outflowing material is less likely to escape the gravitational potential a massive system than a dwarf galaxy (Peeples & Shankar 2011). Furthermore, the scatter in the MZR (~ 0.1 dex) may be driven by a third parameter, including gas fraction (Hughes et al. 2013; Bothwell et al. 2016; Brown et al. 2018; Zu 2020; Chen et al.

* E-mail: yingzu@sjtu.edu.cn

2022), size (Ellison et al. 2008; Yabe et al. 2014), and SFR (Mannucci et al. 2010; Lara-López et al. 2010; Yates et al. 2012; Andrews & Martini 2013). In particular, SDSS galaxies form a tight (~ 0.05 dex) surface $Z_{\text{gas}}(M_*, \dot{M}_*)$ in the 3D parameter space of Z_{gas} , M_* , and \dot{M}_* , dubbed the “fundamental metallicity relation” (FMR; Mannucci et al. 2010; Lara-López et al. 2010). Intriguingly, the observed FMR exhibit little evolution from $z = 0.1$ up to $z=2.5$ (Mannucci et al. 2010; Topping et al. 2021), despite a significant redshift evolution in the amplitude of MZR ($\log O/H \propto (1+z)^{-2.3}$ at fixed mass; Ly et al. 2016).

Although the existence of FMR remains a subject of intense debate (Sánchez et al. 2013; Barrera-Ballesteros et al. 2017; Cresci et al. 2019), various theoretical models have subsequently been proposed to explain the phenomenon and its apparent lack of redshift evolution (Dayal et al. 2013; Forbes et al. 2014; Harwit & Brisbin 2015; Hunt et al. 2016; Kacprzak et al. 2016). The most important among them is a class of CEMs named the “equilibrium” or “gas-regulator” models (Bouché et al. 2010; Davé et al. 2012; Lilly et al. 2013). The equilibrium CEMs assume a constant or slowly-evolving gas reservoir, which implies that the gas accretion rate maintains an instantaneous balance with the rate of gas consumption due to star formation and mass-loaded outflows. In essence, the equilibrium CEMs drive the galaxies to chemical equilibrium so rapidly that the observed metallicity in the ISM has little memory of the past histories of star formation or chemical enrichment, establishing a tight $Z_{\text{gas}}(M_*, \dot{M}_*|z)$ relation at each epoch. Alternatively, however, the apparent constancy of FMR with redshift may emerge out of a non-equilibrium yet somewhat coherent enrichment of star-forming galaxies on the M_* vs. \dot{M}_* plane. To explore a more general CEM that does not assume a steady-state gas reservoir, we develop a non-equilibrium CEM (NE-CEM) that explicitly tracks the variation of metal production, dilution, and ejection over the history of star-forming galaxies.

The success of such an NE-CEM depends critically on the accuracy of *in-situ* SFHs reconstructed from observations. For distant galaxies with unresolved stellar populations, spectral energy distribution (SED) fitting remains the only viable means of reconstructing SFHs (Kauffmann et al. 2003; Walcher et al. 2011; Conroy 2013; Leja et al. 2019), but the large stochasticity in star formation events renders such reconstruction extremely challenging for individual galaxies (Broussard et al. 2019; Tacchella et al. 2020; Iyer et al. 2022; Wang et al. 2022a). The issue can be potentially circumvented by reconstructing the *average* (hence smooth) SFH for a large number of *similar* galaxies, and the lack of sudden bursts is not important for modelling pure core-collapsed supernova (CCSN) elements (e.g., oxygen; Woosley & Weaver 1995; Johnson 2019) due to the short lifetimes of CCSN progenitors (see Johnson & Weinberg 2020, for the impact of bursts on various abundance ratios). Conceptually speaking, the average SFH is the convolution between the average (baryon) mass accretion history (MAH) of their host haloes and a transfer function that characterises the delayed star formation episodes on shorter timescales (Wang et al. 2019). By studying the variability of SFHs in various hydrodynamical simulations and semi-analytic models (SAMs), Iyer et al. (2020) found that the *in-situ* SFHs in different galaxy formation models are all coherent with the MAHs of their parent haloes on long timescales (>3 Gyr). Therefore, given that galaxies with the same M_* and \dot{M}_* observed at $z=0$ should live in similar haloes (Zu & Mandelbaum 2015, 2016, 2018), and that halo MAHs follow a simple, universal profile (van den Bosch 2002; Zhao et al. 2009), we expect the *average in-situ* SFH of those galaxies to be fairly representative of the individual ones. In the current work, we aim to show that using a well-motivated functional form predicted

by the EAGLE simulation allows us to observationally reconstruct robust average *in-situ* SFHs for our NE-CEM analysis.

The key to constraining the physics of stellar feedback-driven outflows lies in robustly measuring the dependence of η on galaxy properties along the SFH, i.e., the mass-loading history (MLH) of galactic outflows. Although there exists a plethora of observations that either directly caught outflows in action from the disks of star-forming galaxies (Rupke 2018, and references therein), or provided indirect evidence via the detection of a significant amount of both metals in the circumgalactic medium (Peeples et al. 2014; Werk et al. 2014; Tumlinson et al. 2017) and dust in the intergalactic medium (Ménard et al. 2010; Zu et al. 2011) around active and even quiescent galaxies (Zhu et al. 2014; Huang et al. 2016; Zu 2021), it is challenging to accurately measure the mass outflow rate \dot{M}_{out} due to the various uncertainties associated with converting column density and wind velocity of some outflowing component (i.e., hot, warm, or cold) into a total mass outflow rate (Murray et al. 2007; Chisholm et al. 2016). Furthermore, direct measurements of η usually require “down-the-barrel” observations of rest-frame ultraviolet (UV) absorption lines from space (Heckman et al. 2015; Chisholm et al. 2018) or deep narrowband imaging of H α emission (McQuinn et al. 2019), which are mostly limited to low-redshift systems. In this paper, we adopt an indirect and complementary approach and reconstruct the MLHs of galactic outflows over the entire lifetime of star-forming galaxies from their observed $Z_{\text{gas}}(M_*, \dot{M}_*)$ relation at $z=0$. Regardless of the epoch, the mass-loading factor of a galaxy should depend on its stellar mass M_* , which sets the depth of gravitational potential, and the specific star formation rate $s\text{SFR}$, which controls the valve of energy and momentum-injection due to stellar feedback. Therefore, we parametrise η at any given epoch as a function of M_* and $s\text{SFR}$ of the galaxy at that epoch, which we are able to predict from the reconstructed SFH in our NE-CEM.

This paper is organised as follows. We develop and calibrate our analytic models of the SFH and MLH by investigating the EAGLE simulation in §2. We then build our NE-CEM by combining the SFH and MLH models and demonstrate the efficacy of NE-CEM using the mock data from the EAGLE simulation in §3. By performing a first-cut NE-CEM analysis using the SDSS metallicity-stellar mass-SFR relation, we derive stringent constraints on the dependence of mass-loading factor on M_* and $s\text{SFR}$ in §4. We also discuss the physical implication of our constraints and the physical cause of the so-called fundamental metallicity relation, before concluding our paper and looking to the future in §5. Throughout this paper, we assume a flat Universe with $\Omega_m=0.306$ and $h=0.677$ for distance and age calculations. We indicate the base-10 logarithm with \lg , and use \dot{M}_* and SFR interchangeably to refer to the star formation rate in the main text and figures, respectively.

2 CHEMICAL ENRICHMENT HISTORY OF GALAXIES IN THE EAGLE SIMULATION

In order to build a robust CEM for galaxies that are not necessarily in equilibrium, we start by systematically investigating the CEH of star-forming galaxies in the EAGLE hydrodynamical simulation. In particular, we firstly develop a compact yet flexible model for the average *in-situ* SFHs of galaxies measured from the EAGLE simulation in §2.1, and then solve the MLHs of galactic outflows by applying a standard one-zone CEM with inflows and outflows (i.e., open-box) along galaxy SFHs in §2.2.

The EAGLE suite of cosmological simulations (Crain et al. 2015; Schaye et al. 2015) constitutes a set of hydrodynamical simulations

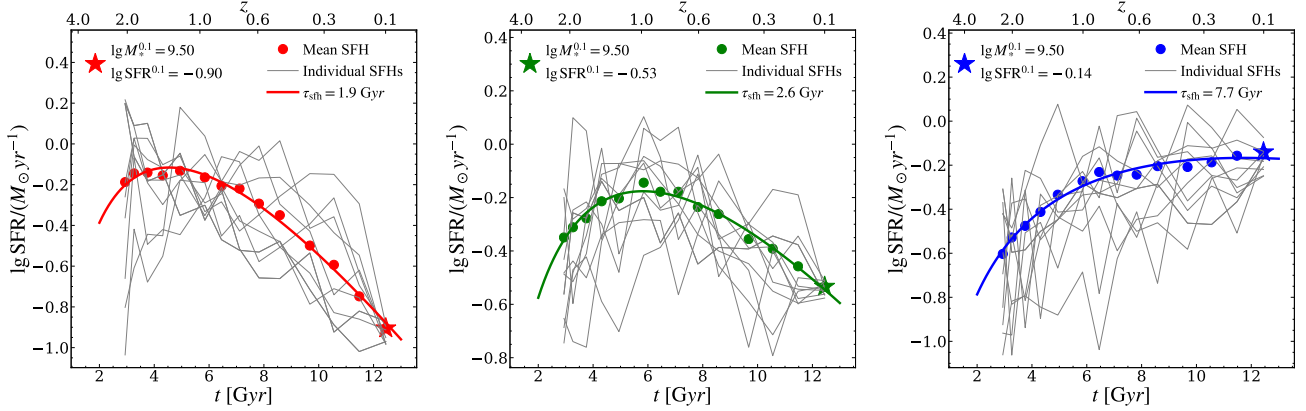


Figure 1. Star formation histories of galaxies in the EAGLE simulation. The three panels are for galaxies observed with the same $M_* = 10^{9.5} M_\odot$ but different \dot{M}_* at $z=0.1$ (i.e., $\text{SFR}^{0.1}$), indicated by the star symbols at $t=12.45$ Gyr. In each panel, the top and bottom x-axes indicate the redshift and time since the big bang, respectively. Thin gray lines show the individual SFHs of ten random galaxies within the same 2D bin of $M_*^{0.1}$ and $\text{SFR}^{0.1}$, while circles represent the mean SFH of all galaxies within that bin. The mean SFH can be well described by the powexp model (solid curve with colour), with the best-fitting value of the SFH timescale τ_{sfh} listed in the top right corner.

run with different box sizes, particle numbers, and sub-grid physics. In this work we employ the “Ref-L100N1504” simulation, which has a periodic box size of 100 Mpc (comoving) and a particle number of 2×1504^3 (i.e., equal number of dark matter and baryonic particles). As a “reference” model, this particular simulation implemented a sub-grid feedback prescription that was calibrated to reproduce the galaxy stellar mass function observed by SDSS at $z=0.1$ (Schaye et al. 2015; Furlong et al. 2015). For further details of the sub-grid implementation in EAGLE, we refer interested readers to Schaye & Dalla Vecchia (2008) for star formation, Dalla Vecchia & Schaye (2012) for stellar feedback and galactic outflows, and Wiersma et al. (2009) for metal enrichment, respectively.

We are primarily concerned with the CEH modelling for star-forming galaxies in the low-to-intermediate stellar mass range ($M_* < 10^{10.2} M_\odot$), where galactic outflows are driven by stellar feedbacks. The star-forming galaxies in the Ref-L100N1504 simulation are broadly consistent with observations at $M_* < \text{a few} \times 10^{10} M_\odot$. In particular, the predicted fraction of star-forming galaxies in the simulation agrees well with the observations at $z=0.1$; The predicted $s\text{SFR}$ of those galaxies are lower than the observations by 0.2–0.3 dex but within the expected systematic errors due to, e.g., the unknown initial mass function (IMF); The metallicity scaling relations predicted by the EAGLE sub-grid model is qualitatively consistent with observations, though the exact slope of the MZR depends on resolution (De Rossi et al. 2017). The overall agreement becomes slightly worse for star-forming galaxies at the higher mass where Active Galactic Nuclei (AGNs) start to dominate the feedbacks. Therefore, the Ref-L100N1504 simulation provides an excellent laboratory for calibrating and testing the SFH and MLH of our analytic NE-CEM regulated by stellar feedbacks. We will refer to the “Ref-L100N1504” simulation simply as the “EAGLE” simulation for the rest of the paper.

2.1 Star formation histories of EAGLE galaxies

As emphasized in the Introduction, a robust reconstruction of the average *in-situ* SFH is key to building an accurate NE-CEM that tracks the production, dilution, and ejection of metals in the ISM. In particular, metal production is directly set by the *in-situ* SFH multiplied by the stellar yield, dilution is associated with the gas

content that is tied with the *in-situ* SFH via the empirical star-forming law (Kennicutt 1998), and ejection is in sync with the *in-situ* SFH via the energy and/or momentum injected after each star formation episode. Therefore, we will measure the individual SFHs for the $z=0.1$ ($t_{0.1}=12.45$ Gyr) galaxies in the EAGLE simulation, in hopes of finding a robust model for the average SFHs. For the sake of brevity, from now on we will refer to the “*in-situ* SFH” simply as “SFH”.

2.1.1 Extracting individual SFH from the merger tree

In order to measure the individual SFHs, we first build a merger tree for each galaxy in the $z=0.1$ output (i.e., snapshot 27) by tracking all of its progenitors in the previous 26 snapshots. In the EAGLE simulation, each halo (including both main and sub-haloes) in EAGLE has a unique GalaxyID and a DescendantID that points to the GalaxyID of its direct descendant in the next snapshot. In an event of a merger, multiple haloes would share the same DescendantID. Since we do not need to explicitly track merger activities in our NE-CEM, we combine multiple progenitors at the same epoch as one synthetic star-forming conglomerate along the SFH. That is, we sum the amount of *in-situ* star formation and stellar mass in all its progenitors at the same epoch to obtain the values of \dot{M}_* and M_* , respectively, for that epoch. In other words, we “collapse” the multiple sub-branches of the merger tree into the main branch, and then measure a total SFH from that single branch. Since major mergers experienced by the star-forming galaxies are rare, the main branch dominates the merger tree in the EAGLE simulation, on average accounting for 96% and 74% of the total stellar mass at $z=0.5$ and $z=2.0$, respectively.

Figure 1 shows the SFHs measured from the EAGLE simulation for galaxies with three different \dot{M}_* but the same $\lg M_* = 9.5$ observed at $z=0.1$ (marked by the star symbols). In each panel, the SFHs of ten random galaxies of the same ($M_*^{0.1}$, $\dot{M}_*^{0.1}$) are shown as individual thin gray lines (with the superscript 0.1 indicating quantities observed at $z=0.1$), while the circles are the mean SFH of these galaxies. As expected in the Introduction, despite the large stochasticity exhibited by individual SFHs, the average SFH of galaxies with the same ($M_*^{0.1}$, $\dot{M}_*^{0.1}$) appears smooth and can thus be well described by an analytic

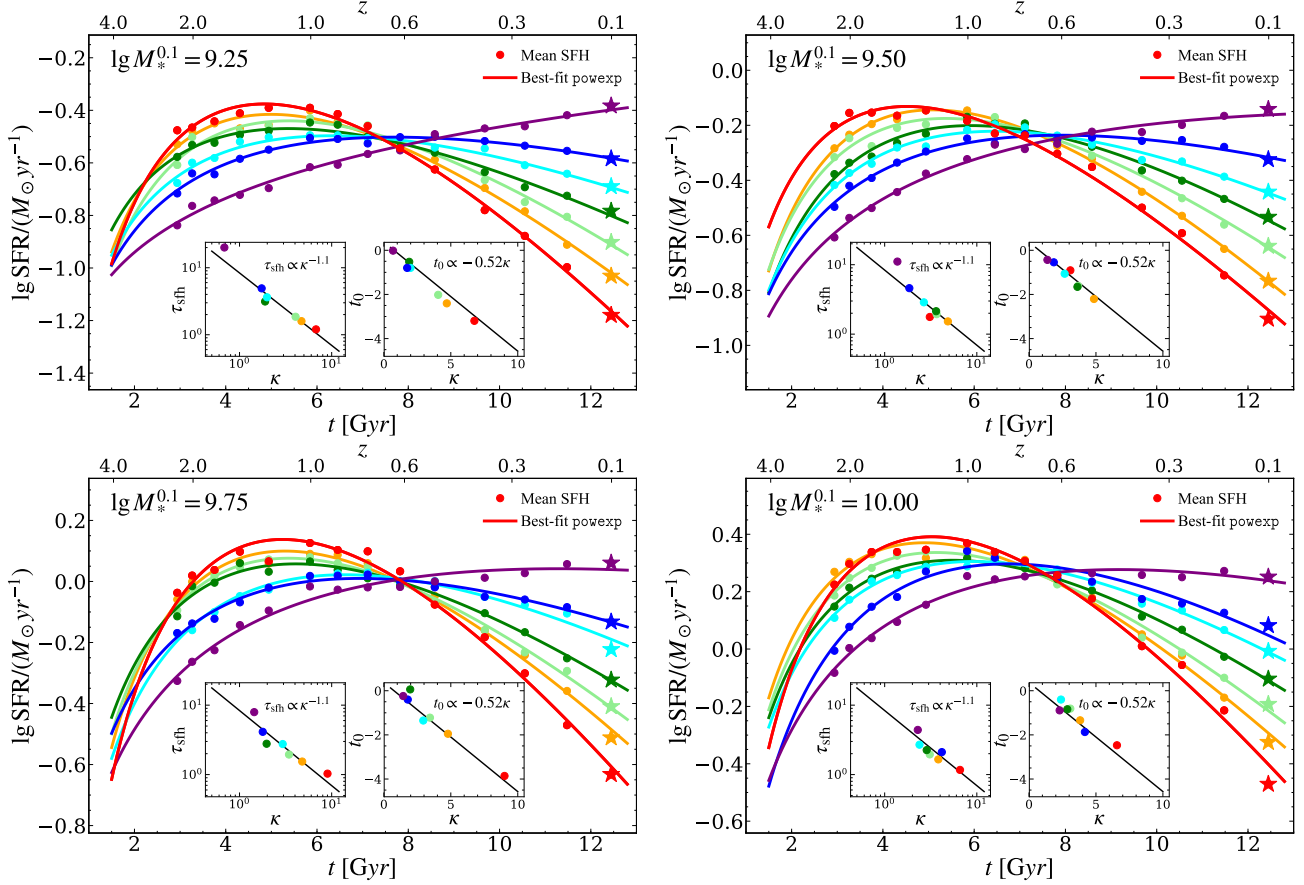


Figure 2. The mean SFHs of EAGLE galaxies with $\lg M_* = 9.25$ (top left panel), 9.5 (top right), 9.75 (bottom left) and 10 (bottom right) observed at $z=0.1$. In each panel, the mean SFHs of galaxies with seven different SFRs observed at $z=0.1$ (star symbols at $t=12.45$ Gyr) are indicated by the circles with seven different colours (increasing $\text{SFR}^{0.1}$ from red to purple), while curves of the matching colours show the best-fitting powexp models of SFH. The top and bottom x-axes indicate the redshift and age of the Universe, respectively. The left and right inset panels show the dependencies of the best-fitting τ_{sfr} and t_0 , respectively, on κ for each of the seven SFHs shown in the main panel (circles with matching colours). Solid line in the left (right) inset panel shows the best-fitting power-law (linear) fit, which is the same across all the stellar mass bins.

function, indicated by the thick colored curve in Figure 1 (as will be discussed further below).

More important, the average SFHs of galaxies with different $\dot{M}_*^{0.1}$ exhibit distinct shapes from one another despite arriving at the same M_* at $z=0.1$. In particular, galaxies with higher $\dot{M}_*^{0.1}$ tend to have a later peak of star formation (compare left and middle panels of Figure 1), while those with the highest $\dot{M}_*^{0.1}$ have yet to reach the peak (right panel of Figure 1). This coherent shape variation of the average SFH with $\dot{M}_*^{0.1}$ indicates that the individual SFH is non-Markovian — the *instantaneous* star formation at the observed epoch *does* retain some memory of its star-forming history in the past. This non-Markovian property of SFH is likely associated with the coherence of SFH with the MAH of haloes on long timescales, a generic prediction of structure formation in the Λ Cold Dark Matter (Λ CDM) cosmology. Therefore, we expect that such non-Markovian property of SFH is present not only in the EAGLE simulation but also in the real Universe, making it plausible to robustly reconstruct the average SFH for SDSS galaxies observed with the same M_* and \dot{M}_* .

2.1.2 Modelling average SFH of galaxies at fixed (M_*, \dot{M}_*)

The reconstruction of SFH from observations requires an accurate fitting formula for the average SFH. After extensive tests, we find

that the “powerlaw-exponential” (hereafter shortened as “powexp”) functional form of Equation 2, which resembles the Schechter function widely used for describing galaxy luminosity functions (see also Katsianis et al. 2021), provides excellent description of the average SFHs measured from EAGLE. It consists of an early power-law increase and a late exponential decline, so that

$$\dot{M}_*(t) = \dot{M}_{*,0} \left(\frac{t-t_0}{\tau_{\text{sfr}}} \right)^\kappa \exp \left(-\frac{t-t_0}{\tau_{\text{sfr}}} \right) \quad (2)$$

where $\dot{M}_{*,0}$ determines the overall amplitude of star formation, t_0 is the starting time of star formation, κ sets the slope of the rapid increase at the onset of star formation, and τ_{sfr} is the characteristic timescale of the exponential decline at late times. Thick solid curves in Figure 1 show the best-fitting models of Equation 2, with the best-fitting values of τ_{sfr} indicated on the top right of each panel. As expected, the characteristic timescale τ_{sfr} increases monotonically with $\dot{M}_*^{0.1}$, yielding $\tau_{\text{sfr}} = 1.9$ Gyr, 2.6 Gyr, and 7.7 Gyr for $\lg \dot{M}_*^{0.1} = -0.9, -0.53, \text{ and } -0.14$, respectively.

Figure 2 demonstrates the efficacy of our powexp SFH model in describing the average SFHs of EAGLE galaxies with $\lg M_*^{0.1} = 9.25, 9.5, 9.75, \text{ and } 10$ in the four panels (arranged by increasing M_* from the top left to the bottom right), with each panel showing the SFHs for galaxies with seven different $\dot{M}_*^{0.1}$ at that M_* (increasing $\dot{M}_*^{0.1}$

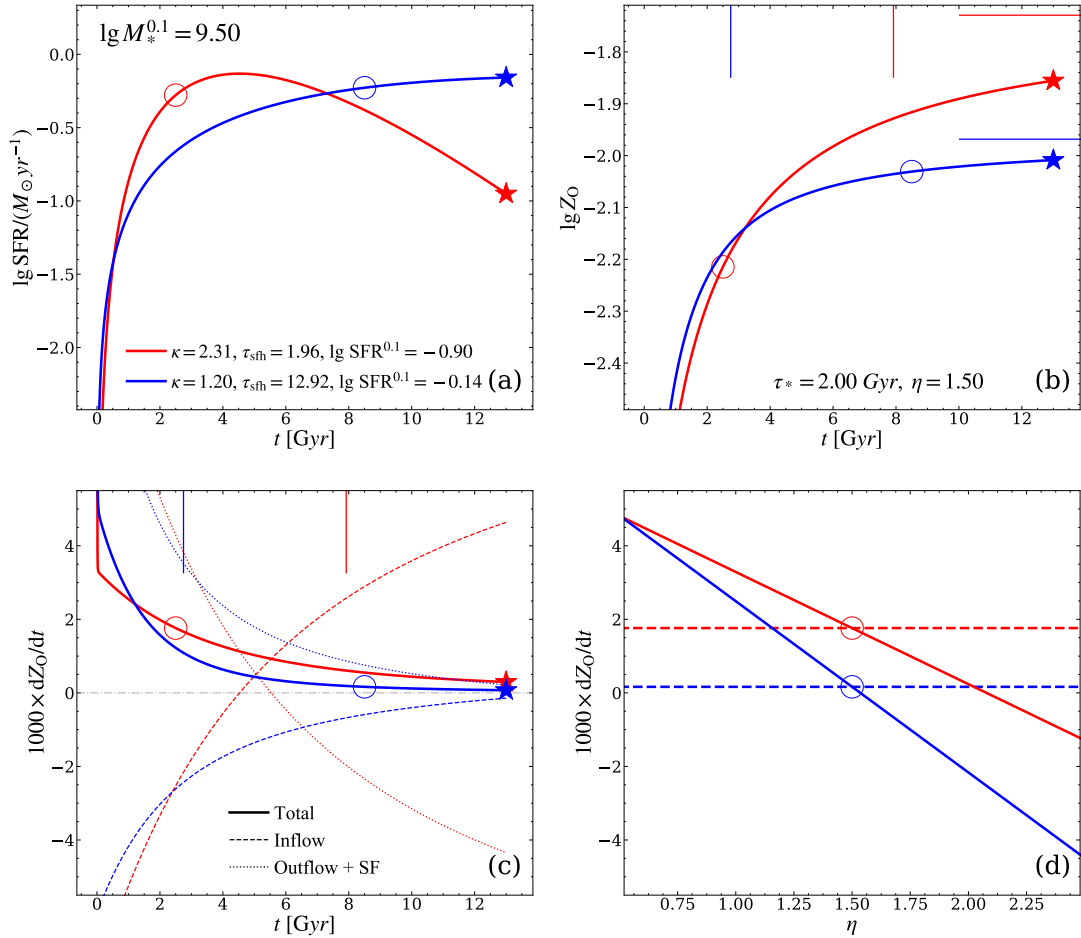


Figure 3. A pedagogical illustration of the different histories of star formation (top left), chemical enrichment (top right), and rate of enrichment dZ_{O}/dt (bottom left) between a typical “young” galaxy (blue) and an “old” galaxy (red) with the same stellar mass of $10^{9.5} M_{\odot}$ observed at $z=0.1$, assuming the `powexp` SFH model with constant gas consumption timescales and mass-loading factors. Bottom right panel illustrates the methodology of our mass-loading reconstruction using two arbitrary epochs for the young (blue circle at $t=8.5$ Gyr) and old (red circle at $t=2.5$ Gyr) galaxies. *Panel (a):* Two example `powexp` SFHs with the parameters listed in the bottom, normalised so that the two galaxies arrive at the same stellar mass of $10^{9.5} M_{\odot}$ by $t=12.45$ Gyr but with different SFRs (stars). *Panel (b):* The two evolution of oxygen abundance Z_{O} as functions of time, predicted by Equation 18 with $\tau_{*}=2$ Gyr and $\eta=1.5$. Horizontal and vertical short lines indicate the equilibrium metallicities ($\lg Z_{\text{O,eq}}=-1.97$ vs. -1.73 for red vs. blue) and timescales (2.75 vs. 7.92 Gyr) predicted by Equation 19 and 17, respectively. *Panel (c):* The total change rates (thick solid curves) of Z_{O} as functions of time predicted by Equation 15, each of which can be decomposed into an “Inflow” component (dashed) and an “Outflow+SF” component (dotted). See text for detail. *Panel (d):* Solid lines are the change rates of oxygen abundance predicted by Equation 15 for different values of η . Horizontal dashed lines indicate the actual values of dZ_{O}/dt at the two epochs indicated by the circles in panels (a), (b), and (c). The intersection points between the solid and dashed lines indicate the correct values of $\eta=1.5$.

from red to purple, as indicated by the stars at $z=0.1$). Similar to Figure 1, solid circles are the average SFHs measured from EAGLE, while solid curves of the same colour indicate the best-fitting `powexp` model of Equation 2. Overall, the best-fitting `powexp` models provide excellent description of the average SFHs measured directly from the EAGLE simulation for star-forming galaxies with $M_{*}^{0.1}$ between roughly $10^9 M_{\odot}$ to $10^{10} M_{\odot}$, similar to the stellar mass range that we aim to explore in the SDSS data. We do not extend our model to galaxies of even higher M_{*} because we want to limit our analysis to the regime of stellar feedbacks, while the outflows in those high- M_{*} systems are progressively driven by AGNs.

The `powexp` SFH model of Equation 2 has four free parameters, while in the observation we usually have only two measured quantities, i.e., M_{*} and \dot{M}_{*} at the observed epoch. Ideally, one would stack the spectra of the observed galaxies at fixed M_{*} and \dot{M}_{*} , and apply the `powexp` SFH to SED-fitting techniques to derive the other two parameters κ and τ_{sfb} (Chen et al. *in prep*). However, for the purpose

of our first-cut analysis, it would be useful to find an empirical constraint to reduce the number of degrees of freedom without resorting to sophisticated machineries like SED-fitting.

The inset panels in Figure 2 point to a promising path to such an empirical constraint. In each panel, the left and right inset panels show the relations between the best-fitting values of κ and those of τ_{sfb} and t_0 , respectively. Note that we allow the values of t_0 to be negative to better fit the shapes of the SFHs at $z \sim 2$, above which we cannot obtain meaningful \dot{M}_{*} measurements from the simulation. The colours of the circles are matched to those of the best-fitting SFH curves in the main panel. Black solid lines are the same across all the inset panels of τ_{sfb} vs. κ , indicating the best-fitting power-law relation $\tau_{\text{sfb}}=0.92\kappa^{-1.1}$. Likewise, black solid lines in the inset panels of t_0 vs. κ are the best-fitting line relation $t_0=-0.52\kappa+0.37$. Since both black solid lines provide reasonably good fits to the respective relations between best-fitting parameters, we assume that the three

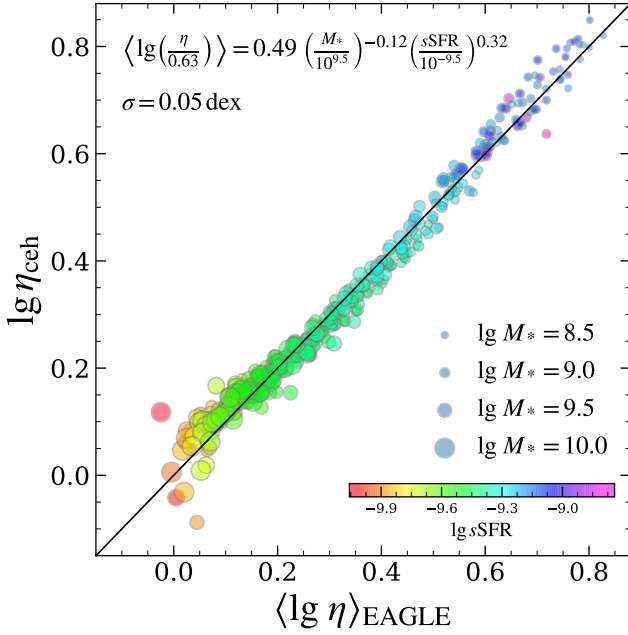


Figure 4. Comparison between the average mass-loading factors reconstructed from CEHs (y-axis) and that predicted from the best-fitting model (x-axis) of Equation 20 (indicated by the equation in the top left corner) for the EAGLE galaxies. The colour and size of each circle represent the $s\text{SFR}$ and M_* of each galaxy, indicated by the colourbar and legends, respectively, in the bottom right. The circles are consistent with the solid diagonal line that indicates the one-to-one relation with a scatter of 0.05 dex.

parameters of Equation 2 roughly follow a power-law relation

$$\lg \tau_{\text{sfr}} = A_\tau \lg \kappa + B_\tau, \quad (3)$$

and a linear relation

$$t_0 = A_0 \kappa + B_0, \quad (4)$$

simultaneously. In essence, galaxies that start forming stars earlier tend to experience faster growth during the power-law phase (Equation 4), and then more rapid declines in the exponential phase (Equation 3). Such tendency of galaxy SFHs is consistent with that of halo MAHs in ΛCDM , where older haloes usually experience faster early-time growth when the Universe was dense than their younger counterparts of the same mass (Zhao et al. 2009). Therefore, we expect the power-law (Equation 3) and linear scaling relations (Equation 4) to be roughly applicable in the real Universe, but likely with a different set of $\{A_\tau, B_\tau, A_0, B_0\}$.

Finally, given that the average M_* and \dot{M}_* of a large sample of galaxies at some observed epoch t_{obs} are usually well measured (e.g., as M_*^{obs} and \dot{M}_*^{obs}), we can change the variables so that

$$\dot{M}_*(t) = \dot{M}_*^{\text{obs}} \left(\frac{t - t_0(\kappa)}{t_{\text{obs}} - t_0(\kappa)} \right)^\kappa \exp \left(\frac{t_{\text{obs}} - t}{\tau_{\text{sfr}}(\kappa)} \right), \quad (5)$$

where we make use of Equation 3 and 4 to obtain $\tau_{\text{sfr}}(\kappa)$ and $t_0(\kappa)$, respectively. On the other hand, κ can be separately derived from the $s\text{SFR}$ at t_{obs} . Analytically integrating Equation 2, we have

$$\frac{M_*^{\text{obs}}}{\dot{M}_*^{\text{obs}}} = \frac{(1-r)\tau_{\text{sfr}}^{\kappa+1} \gamma \left(\kappa + 1, \frac{t_{\text{obs}} - t_0}{\tau_{\text{sfr}}} \right)}{(t_{\text{obs}} - t_0)^\kappa \exp \left(-\frac{t_{\text{obs}} - t_0}{\tau_{\text{sfr}}} \right)} \equiv \mathcal{F}(\kappa), \quad (6)$$

where γ is the incomplete Gamma function and r is the IMF-averaged recycle fraction, defined as the fraction of mass formed into stars that

is returned to the ISM by supernovae and evolved stars. The value of κ can thus be solved trivially from the inverse function of \mathcal{F} as $\kappa = \mathcal{F}^{-1}(M_*^{\text{obs}}/\dot{M}_*^{\text{obs}})$. In this way, we can analytically derive the average SFH from any combination of M_*^{obs} and \dot{M}_*^{obs} , for any given set of $\{A_\tau, B_\tau, A_0, B_0\}$.

2.2 Chemical Evolution along the average SFH

2.2.1 Standard CEM with the powexp SFH

Armed with the powexp SFH model developed in §2.1, we are now able to analytically track the oxygen abundance in the ISM by applying an open-box CEM along any given powexp SFH. In the standard instantaneous recycling approximation and the notations of Weinberg et al. (2017), the evolution equation for the total mass of oxygen in the ISM M_{O} is

$$\dot{M}_{\text{O}} = m_{\text{O}}^{\text{cc}} \dot{M}_* - (1-r)Z_{\text{O}} \dot{M}_* - \eta Z_{\text{O}} \dot{M}_*, \quad (7)$$

where r is the recycle fraction, $Z_{\text{O}} \equiv M_{\text{O}}/M_{\text{gas}}$ is the current oxygen abundance by mass in the ISM, m_{O}^{cc} is the IMF-averaged oxygen yield, defined as the mass of oxygen produced and returned to the ISM per solar mass of star formation (i.e., oxygen yield per stellar generation, as opposed to the net yield y_{O}). For the Chabrier stellar IMF assumed in EAGLE, we adopt recycle fraction $r=0.4$ and oxygen yield $m_{\text{O}}^{\text{cc}}=0.022^1$. In Equation 7, the first term represents oxygen production rate by core-collapsed supernovae (CCSNe), the second term combines the depletion rate of oxygen previously in the ISM into stars and the recycling rate of oxygen originally locked in the stars back into the ISM, and the third term describes the ejection of oxygen by galactic outflows, with a mass-loading factor η , the key parameter that we want to constrain in this paper.

Although Equation 7 assumes the metallicity of the ejecta Z_{O}^{ej} is the same as the ISM (i.e., outflowing gas is pure ISM), over-enriched outflows (i.e., ISM entrainment fraction is below unity) can be accounted for by substituting the metal-loading factor ζ (Peebles & Shankar 2011)

$$\zeta \equiv \frac{Z_{\text{O}}^{\text{ej}} \dot{M}_{\text{out}}}{Z_{\text{O}} \dot{M}_*} \quad (8)$$

for η in our formulae.

Considering an evolving gas reservoir, the change rate of oxygen abundance is thus

$$\frac{dZ_{\text{O}}}{dt} = \frac{\dot{M}_{\text{O}}}{M_{\text{gas}}} - \frac{\dot{M}_{\text{gas}}}{M_{\text{gas}}} Z_{\text{O}}, \quad (9)$$

where the first term represents the change of Z_{O} from the variation of oxygen mass due to star formation and galactic outflows, while the second term describes the dilution due to gas inflow. We assume the metallicity of inflowing gas is primordial in this paper.

By further defining the gas consumption timescale $\tau_* \equiv M_{\text{gas}}/\dot{M}_*$, we can write out the change rate of oxygen abundance

$$\frac{dZ_{\text{O}}}{dt} = \frac{m_{\text{O}}^{\text{cc}}}{\tau_*} - \frac{Z_{\text{O}}}{\tau_{\text{dep}}} - \left(\frac{\dot{M}_*}{\dot{M}_*} + \frac{\dot{\tau}_*}{\tau_*} \right) Z_{\text{O}}, \quad (10)$$

¹ We adopt an upper mass cutoff of the Chabrier IMF as $m_{\text{up}}=80 M_{\odot}$, and derive a net yield of $y_{\text{O}}=0.0367$ based on the Fig. 5 of Vincenzo et al. (2016). We then multiply y_{O} by $(1-r)=0.6$ to obtain $m_{\text{O}}^{\text{cc}}=0.022$. We note that as Griffith et al. (2021) pointed out, the value of m_{O}^{cc} could vary by a factor of three even at fixed IMF depending on the assumptions about blackhole formation.

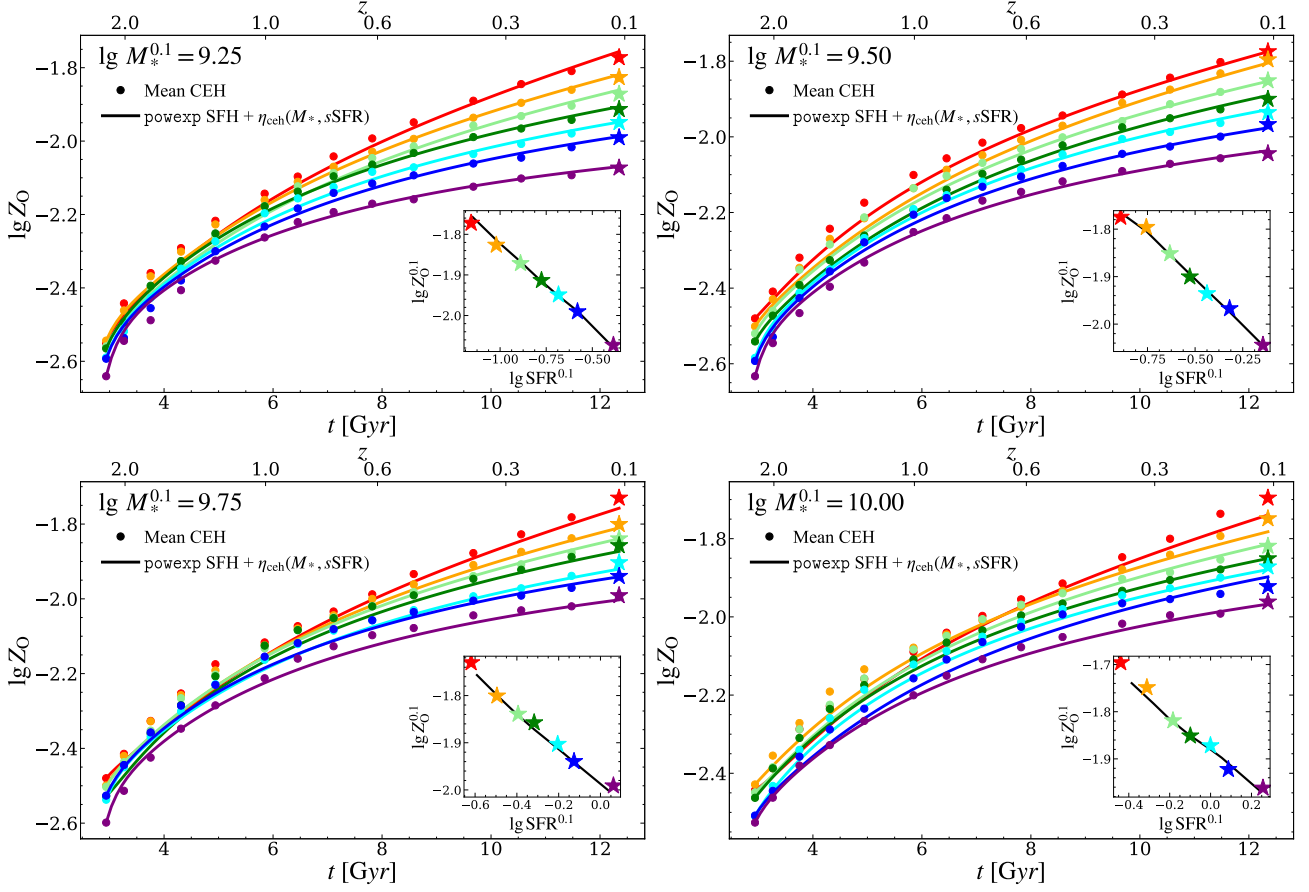


Figure 5. Similar to Figure 2, but for the CEHs. In each panel, coloured circles are the mean CEHs measured from the EAGLE simulation, which can be well described by the solid curves with matching colours, predicted by the combination of the best-fitting models of powexp SFHs and η_{ceh} from Equation 20. Inset panels highlight the agreement between the mock measurements from the simulation (stars) and the best-fitting model predictions (solid black line) at $z=0.1$.

where

$$\tau_{\text{dep}} \equiv \tau_* / (1 + \eta - r) \quad (11)$$

is the gas depletion timescale. For the powexp SFH, we have

$$\frac{\dot{M}_*}{M_*} = \frac{\kappa}{t - t_0} - \frac{1}{\tau_{\text{sFH}}}. \quad (12)$$

We also assume a scaling relation between \dot{M}_* and M_{gas} similar to the Schmidt law (Schmidt 1959),

$$M_{\text{gas}} = M_{g,0} \dot{M}_*^\epsilon, \quad (13)$$

which provides a good description of the gas reservoir in EAGLE galaxies (as it was put in by hand, see Schaye & Dalla Vecchia 2008), so that

$$\frac{\dot{\tau}_*}{\tau_*} = (\epsilon - 1) \frac{\dot{M}_*}{M_*}. \quad (14)$$

Plugging Equation 12 and 14 into Equation 10, we arrive at

$$\frac{dZ_O}{dt} = \left[\frac{m_O^{\text{cc}}}{\tau_*} - \frac{Z_O}{\tau_{\text{dep}}} \right] + \left[\frac{\epsilon Z_O}{\tau_{\text{sFH}}} - \frac{\epsilon \kappa Z_O}{t - t_0} \right]. \quad (15)$$

where the term in the first bracket modifies M_O through the combination of stellar nucleosynthesis, recycling, and outflows, and the second bracket modifies M_{gas} through inflows. We refer to the first and second bracketed terms as ‘‘Outflow+SF’’ and ‘‘Inflow’’, respectively, in our later analysis of the conditions for chemical equilibrium.

In addition, Equation 15, or more generally Equation 9, serves as the basis for our method of measuring the strength of outflows from hydrodynamic simulations, as $\eta(t)$ is the only unknown parameter in the equation that cannot be measured from simulations in a straightforward manner. We will expand on the method in detail in §2.2.3.

Setting $\kappa=0$ and $\epsilon=1$ correspond to the commonly adopted model of a pure exponential SFH with constant τ_* , reducing Equation 15 to a simpler form

$$\frac{dZ_O}{dt} = \frac{m_O^{\text{cc}}}{\tau_*} - \frac{Z_O}{\tau_{\text{dep}}} + \frac{Z_O}{\tau_{\text{sFH}}} = \frac{m_O^{\text{cc}}}{\tau_*} - \frac{Z_O}{\tilde{\tau}}, \quad (16)$$

where for the second equality we have adopted the ‘‘harmonic difference timescale’’

$$\tilde{\tau} \equiv \frac{1}{\tau_{\text{dep}}^{-1} - \tau_{\text{sFH}}^{-1}}, \quad (17)$$

introduced by Weinberg et al. (2017).

2.2.2 The simple case: constant τ_* and η

Before measuring the time-dependent τ_* and η in the EAGLE simulation, we firstly apply our powexp SFH model to the standard CEM assuming constant values of τ_* and η . This simple case serves as the baseline model against which we compare our comprehensive NE-CEM in §3.2.

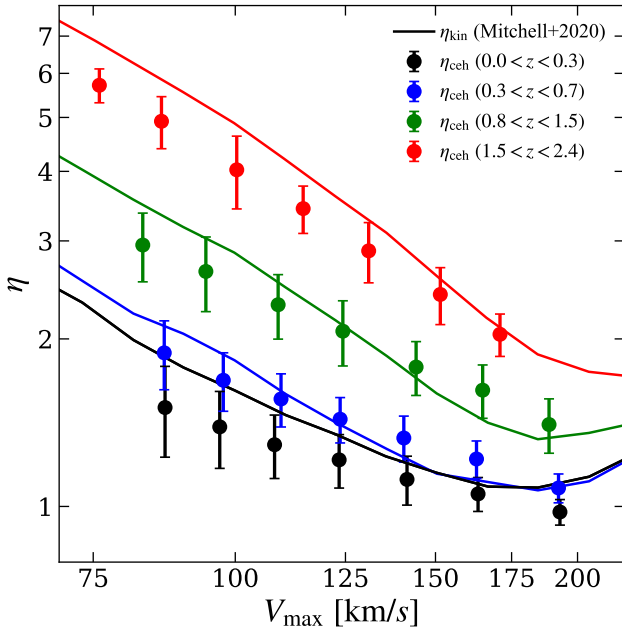


Figure 6. Comparison between the dependences of the mass-loading factor on the halo maximum circular velocity measured chemically by our method (circles with errorbars) and kinematically by Mitchell et al. (2020) (solid curves of matching colours) for EAGLE galaxies in four different redshift bins, listed by the legend in the top right. The good agreement between the two measurements using entirely different methods is quite remarkable.

Assuming constant η , we can numerically integrate Equation 10 to obtain the time evolution of Z_O , and by further assuming a constant τ_* by setting $\epsilon=1$, the integration becomes analytic, yielding

$$Z_O(t) = m_O^{cc} \frac{\tilde{\tau}}{\tau_*} \left(\frac{t}{\tilde{\tau}}\right)^{-\kappa} \exp\left(\frac{t}{\tilde{\tau}}\right) \gamma\left(\kappa + 1, \frac{t}{\tilde{\tau}}\right). \quad (18)$$

At $t \gg \tilde{\tau}$, this system would approach an equilibrium metallicity of

$$Z_{O,eq} = m_O^{cc} \frac{\tilde{\tau}}{\tau_*}, \quad (19)$$

which is a generic prediction of CEMs with constant η and τ over an exponential declining tail of star formation (Weinberg 2017).

Figure 3 shows the average SFHs, CEHs, and the evolutions of dZ_O/dt in panel (a), (b), and (c), respectively, for two typical galaxies with the same $\lg M_*^{0.1}=9.5$ but different $\lg \dot{M}_*^{0.1}$ of -0.9 (red star) and -0.14 (blue star), assuming constant values of $\eta=1.5$ and $\tau_*=2$ Gyr. In panel (a), the old galaxy (red curve; $\kappa=2.31$, $\tau_{sfh}=1.96$ Gyr) has an early peak in its SFH and is almost quenched by $z=0.1$, whereas the young galaxy (blue curve; $\kappa=1.2$, $\tau_{sfh}=12.92$ Gyr) has yet to reach peak star formation by $z=0.1$. This difference between the two SFH shapes directly leads to two different trajectories of chemical evolution in panel (b), where blue and red horizontal dashed lines indicate the equilibrium metallicities $\lg Z_{O,eq}=-1.73$ and -1.97 (Equation 19) of the young and old galaxies, respectively. Meanwhile, blue and red vertical lines indicate the corresponding equilibrium timescales $\tilde{\tau}$ of the young and old galaxies, respectively, indicating that the young galaxy ($\tilde{\tau}=2.75$ Gyr) approaches chemical equilibrium in a faster pace than its older counterpart ($\tilde{\tau}=7.92$ Gyr). Compared to their lifetimes until $z=0.1$ (12.45 Gyr), however, the two equilibrium timescales of both galaxies are rather short.

The details of the CEHs are better illustrated by their differential form in panel (c), where the solid, dashed, and dotted curves indicate the total dZ_O/dt (Equation 15), “Outflow+SF” ($m_O^{cc}/\tau_* - Z_O/\tau_{dep}$),

and “Inflow” ($Z_O/\tau_{sfh} - \kappa Z_O/(t - t_0)$) components of dZ_O/dt , respectively. We note that CEHs in this work refer to the evolution of Z_O instead of M_O . Both total change rates of Z_O rapidly approach zero, i.e., reaching chemical equilibrium, after their respective equilibrium timescales $\tilde{\tau}$ indicated by the vertical lines on top. However, the two galaxies are enriched in distinct manners. For the young galaxy, the contribution from the “Outflow+SF” component is always positive before $t_{0.1}=12.45$ Gyr and vice versa for the “Inflow” component, whereas for the old galaxy the signs are reversed at large t . The reason is as follows. The young galaxy is enriched more slowly (hence lower Z_O), with a longer τ_{sfh} , and larger κ than the old ones, but the two galaxies have the same τ_* and τ_{dep} , leading to $Z_O^{young} < m_O^{cc} \tau_{dep}/\tau_* < Z_O^{old}$ and $\tau_{sfh}^{young} \kappa^{young} > t > \tau_{sfh}^{old} \kappa^{old}$ simultaneously when $t_1 > t \gg t_0$. In essence, for the young galaxy, metal production overwhelms metal ejection due to the overall low level of enrichment in the ISM, while metal dilution is effective due to the ample inflow of pristine gas. The situation for the old galaxy is reversed — metal production due to waning star formation cannot keep up with the metal loss due to outflows loaded with highly-enriched ISM, while metal dilution turns into metal concentration as the meager inflow cannot catch up with the rate at which the gas is consumed. At $t \gg t_1$, however, the “Outflow+SF” term of young galaxy will cross zero and becomes negative as Z_O keeps increasing, while the “Inflow” term instead becomes positive, leading to similar trajectories as the old galaxy. Eventually, both components conspire to reach equilibrium metallicity $Z_{O,eq}$, following the exponentially declining \dot{M}_* regardless of their early SFHs.

Finally, panel (d) of Figure 3 demonstrates that the value of η can be solved from the combination of SFH (top left) and CEH (top right) using Equation 15 (bottom left). Red and blue circles mark two random epochs of 2.5 Gyr and 8.5 Gyr for the old and young galaxies, respectively (also shown across the other three panels of Figure 3). Solid red (blue) line shows the variation of dZ_O/dt as a function of η at 2.5 Gyr (8.5 Gyr) for the old (young) galaxy, given by Equation 15. Horizontal dashed lines indicate the true values of dZ_O/dt measured from the CEHs (horizontally aligned with the circles in panel (c)). Therefore, the intersections between the solid and dashed lines of the same colour yield the correct values of η (i.e., the x-axis value of the circles, $\eta=1.5$) that are required by the consistency between the SFH and CEH of the same galaxy at that particular epoch. Next we will apply this method to the EAGLE simulation to reconstruct the MLHs of outflows in EAGLE.

2.2.3 Modelling mass-loading histories $\eta(t)$ in EAGLE

To explore robust modelling of η that can describe the galactic winds in the EAGLE simulation and in the observations, we first need to reconstruct the average MLHs of EAGLE galaxies from their CEHs. For this purpose, we develop a novel method to accurately measure η chemically and describe the method in detail below. Although developed with the EAGLE simulation in mind, the method can be easily applied to any hydrodynamical simulation that explicitly tracks oxygen in the ISM.

For each of the 28 bins of fixed $M_*^{0.1}$ and $\dot{M}_*^{0.1}$ in Figure 1, we firstly measure the sum of the star-forming gas mass $M_{gas}(t)$ (MasType_Gas) and the sum of oxygen mass in the star-forming gas $M_O(t)$ (SF_Mass×SF_Oxygen) from all the progenitors at each of the 14 outputs between $z=2.24$ and $z=0.1$, using the merger trees built in §2.1.1. Secondly, from the measured $M_{gas}(t)$ and $M_O(t)$ we can compute $Z_O(t)$ as well as its derivative $dZ_O/dt(t)$ from the smooth CEH derived from quadratically interpolating Z_O over the 14

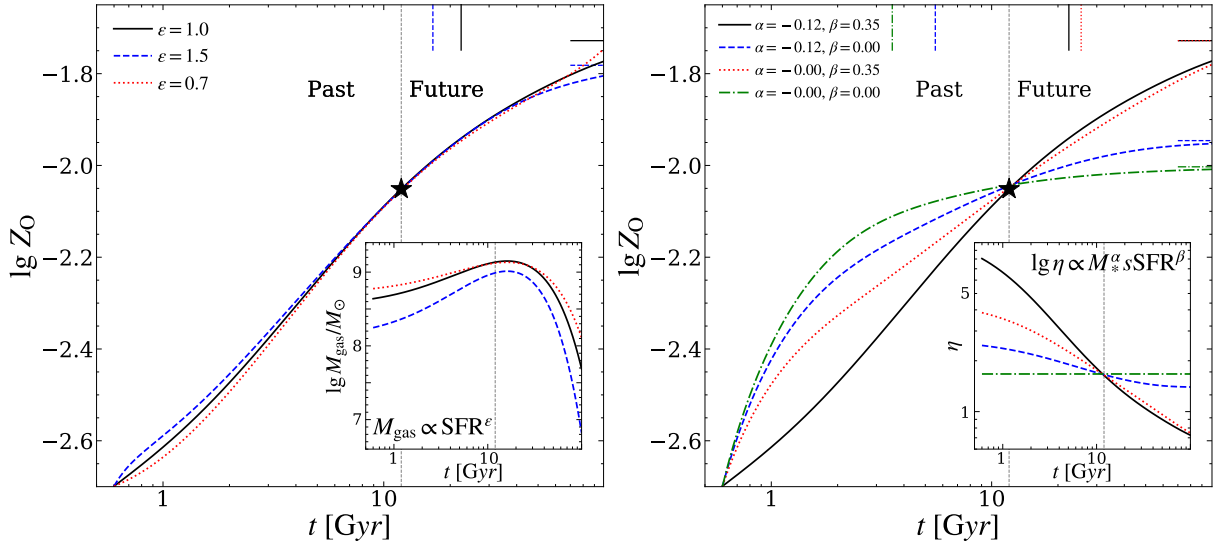


Figure 7. Impact of ϵ (left panel) and the combination of α and β (right panel) on the chemical evolution of a typical galaxy from birth to $t=100$ Gyr. The SFH of the galaxy is the same as that of the “young” galaxy in the panel (a) of Figure 3. In each panel, we adjust the normalizations of M_{gas} (left) or η (right) so that the trajectories of chemical enrichment all pass through the same value of Z_0 today at $t=12.45$ Gyr. In the left panel, black solid, blue dashed, and red dotted curves indicate the different chemical enrichment trajectories assuming $\epsilon=1$ (i.e., constant τ_*), 1.5, and 0.7, respectively. The inset panel on the left shows the corresponding evolutions of M_{gas} . In the right panel, black solid, blue dashed, red dotted, and green dot-dashed curves indicate the predicted chemical enrichment from $(\alpha, \beta)=(-0.12, 0.35)$, $(-0.12, 0)$, $(0, 0.35)$, and $(0, 0)$ (i.e., constant η), respectively. Horizontal and vertical short lines in each panel indicate the corresponding equilibrium metallicities and timescales of the CEHs (except for $\epsilon=0.7$ in which case the galaxy could never reach chemical equilibrium).

snapshots. Lastly, we solve for $\eta(t)$ by applying the measured quantities to Equations 7 and 9, following the methodology illustrated in the panel (d) of Figure 3. Similar to the practice in the SFH measurements, we employ the “collapsed” tree to compute an effective mass-loading factor for the synthetic progenitor in each epoch. To avoid confusion when comparing with the η measured by other techniques in §2.2.4, we refer to our mass-loading factors derived from the CEHs as η_{ceh} . In total, we have obtained η_{ceh} measurements for $14 \times 28=392$ average galaxies, i.e., 14 epochs for each of the 28 bins of galaxies at fixed $M_*^{0.1}$ and $\dot{M}_*^{0.1}$.

As discussed in the Introduction, the mass-loading factor of a galaxy should depend on the galaxy internal properties, and its apparent variation with redshift is due to the redshift evolution of those internal properties. The most important among them are the stellar mass M_* , which determines the strength of the gravitational potential, and the specific star formation rate $s\text{SFR}$, which is associated with the specific injection rate of energy and/or momentum that drive the galactic winds. Therefore, we build a simple empirical model of $\eta_{\text{ceh}}(t)$ by parametrising $\lg \eta_{\text{ceh}}(t)$ as the product of two power-laws of $M_*(t)$ and $s\text{SFR}(t)$,

$$\lg \left(\frac{\eta}{\eta_0} \right) = f \left(\frac{M_*}{M_{*,0}} \right)^\alpha \left(\frac{s\text{SFR}}{s\text{SFR}_0} \right)^\beta, \quad (20)$$

where f is the overall normalization parameter, and we fix the three pivot values to $\lg \eta_0 = -0.2$, $\lg M_{*,0} = 9.5$, and $\lg s\text{SFR}_0 = -9.5$ throughout this paper. Note that the parameterisation in Equation 20 implies that η is always greater than $\eta_0 = 0.631$, which should be comfortably lower than the mass-loading factors in star-forming galaxies below a few $\times 10^{10} M_\odot$, and even more so considering the outflows are likely more enriched than the ISM (i.e., ζ is always greater than η).

The two slopes of the power-laws in Equation 20 are the key parameters that we aim to constrain from observations in this paper. In particular, α is the slope of (log) mass-loading dependence on

stellar mass, where simple theoretical arguments expect $\eta \propto M_*^{-1/3}$ for momentum-conserving winds (Murray et al. 2005) and $\eta \propto M_*^{-2/3}$ for energy-conserving winds (Chevalier & Clegg 1985; Heckman et al. 1990); β is the slope of the $s\text{SFR}$ -dependence. For stochastic explosion of isolated massive stars in the low- $s\text{SFR}$ regime, the outflows are highly inefficient with low η because most supernova remnants radiate significant energy away before breaking out of the galactic discs (Koo & McKee 1992; Murray et al. 2011). However, in starburst systems the stellar explosions are temporally correlated and spatially clustered (Gentry et al. 2017; Yadav et al. 2017; Gentry et al. 2019), thereby driving superbubbles that rapidly break out of the discs and power strong galactic outflows with high η ((Kim et al. 2017; Yadav et al. 2017; Vasiliev et al. 2017; Fielding et al. 2018). Roughly speaking, the measurement of α provides useful constraints on the wind driving mechanism, whereas the β measurement could probe the impact of clustered supernovae on stellar feedback.

We perform a multiple linear regression analysis using Equation 20 over the 392 sets of η_{ceh} , M_* , and $s\text{SFR}$ measurements (assuming equal weights), yielding the best-fitting values of $f = 0.45 \pm 0.01$, $\alpha = -0.15 \pm 0.02$, and $\beta = 0.34 \pm 0.02$. Figure 4 compares the predictions (x-axis) from the best-fitting model of Equation 20 (indicated in the top left corner) to the η_{ceh} directly inferred from the CEHs (y-axis) for the 392 systems in EAGLE (circles). The colour and size of each circle represent the $s\text{SFR}$ and M_* of the galaxy indicated by the colourbar and legend in the bottom right corner, respectively. The circles are mostly aligned with the black diagonal line (i.e., the one-to-one relation), showing that Equation 20 is a good model for describing the mass-loading factors in the EAGLE simulation at all redshifts.

Figure 5 demonstrates the efficacy of our best-fitting model of η_{ceh} when combined with the powexp SFH in predicting the CEHs of EAGLE galaxies. The four panels compare the CEHs directly measured from EAGLE (circles) with those predicted by the combined model

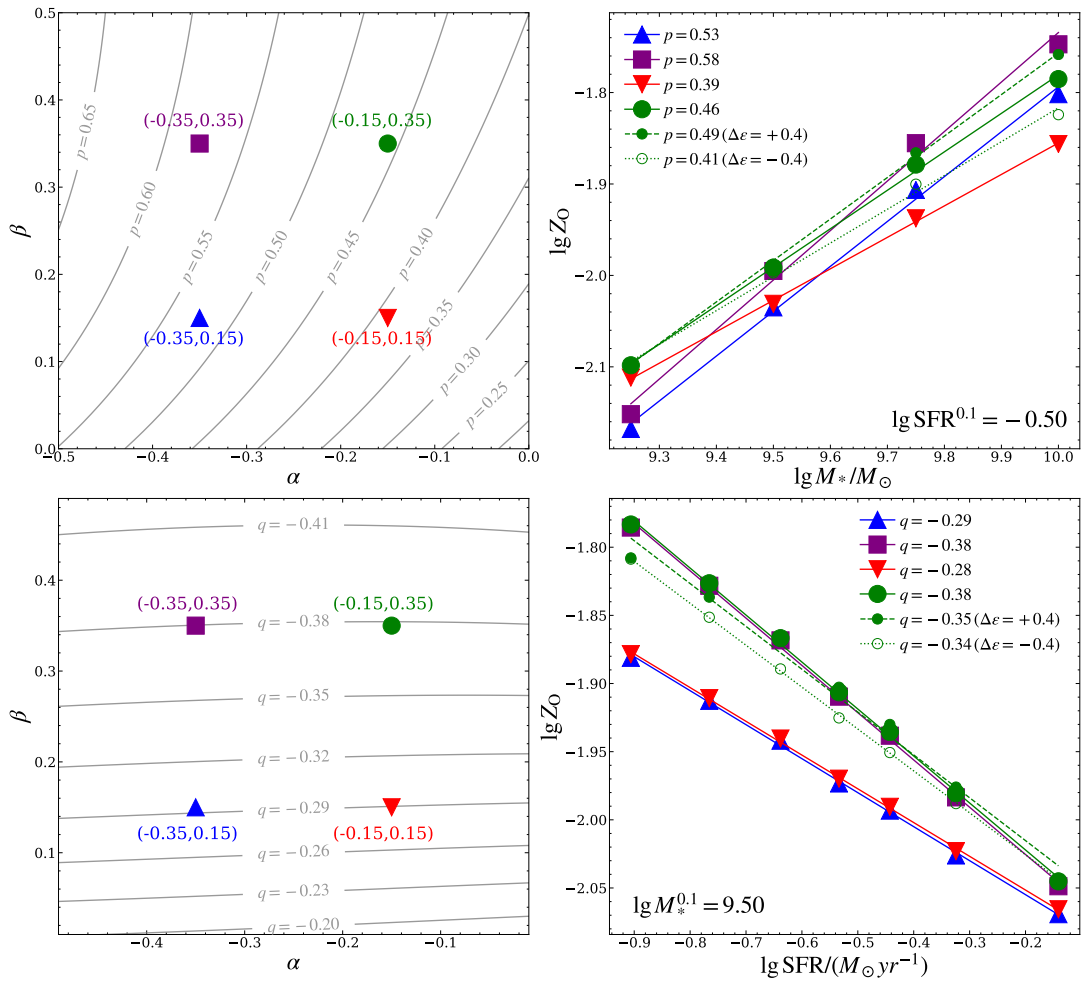


Figure 8. Connection between the slope parameters of η (α and β) and the slope of the $Z_{\text{O}}-M_*$ relation at fixed SFR (p ; top row) or the slope of the $Z_{\text{O}}-\text{SFR}$ relation at fixed M_* (q ; bottom row), predicted by the fiducial NE-CEM for EAGLE galaxies at $z=0.1$. In each row, the left panel shows the iso- p contours predicted by the fiducial NE-CEM on the 2D plane of α vs. β with all other parameters fixed, while the right panel shows the predicted $Z_{\text{O}}-M_*$ relations at $\lg \text{SFR}=-0.5$ (top) or the predicted $Z_{\text{O}}-\text{SFR}$ relations at $\lg M_*=9.5$ (bottom) for four different combinations of α and β (solid lines through large symbols) indicated by the four coloured symbols in the left panel (with the parameter values displayed inside the parentheses). The measured values of the slopes are indicated by the legends on the top left. In addition, dashed and dotted lines through the small green filled and open circles in the right panel indicate the predicted relations after perturbing the fiducial value of $\epsilon=0.91$ by $+0.4$ and -0.4 , respectively.

of the best-fitting η_{ceh} from Equation 20 and the powexp SFHs, for the same sets of galaxy samples defined in Figure 2. In each inset panel, we show the oxygen abundance at $z=0.1$ as a function of $\dot{M}_*^{0.1}$ directly measured from the simulation (stars), which is successfully predicted by the best-fitting combined model (black solid curve). Overall, the predicted CEHs are in good agreements with the direct measurements, especially at $z=0.1$ where the $Z_{\text{O}}(M_*, \dot{M}_*)$ relation is an observable in the mock test of §3.4.

2.2.4 Comparison with Mitchell et al. (2020): η_{ceh} vs. η_{kin}

To further validate our reconstruction of the MLHs of outflows, we can compare our chemically-inferred η_{ceh} with the mass-loading factors directly measured from counting the wind particles in the EAGLE simulation. However, direct measurement of η in hydrodynamic simulations is never straightforward, primarily because η is often not a direct parameter put in by hand (though could be set at injection; see e.g., Pillepich et al. 2018), but requires a careful but somewhat arbitrary identification and tracking of wind particles. In

particular, to measure the mass loading factors in the same EAGLE simulation employed by this work, Mitchell et al. (2020) firstly identified the ISM particles by including the star-forming gas and some dense portion of the non-star-forming gas, and then from those ISM particles selected galactic wind particles as those with time-averaged radial velocities higher than one quarter of the maximum circular velocity of the halo V_{max} and instantaneous radial velocities above $V_{\text{max}}/8$. We hereafter refer to the mass-loading factors measured by Mitchell et al. (2020) using this kinematic criteria as η_{kin} , as opposed to η_{ceh} we measured chemically in §2.2.3.

Figure 6 compares our chemically-measured η_{ceh} (circles with errorbars) with the kinematically-measured η_{kin} by Mitchell et al. (2020) (solid curves) in four different redshift bins between $z=0$ and $z=2.4$. The redshift binning exactly follows that in the Fig. 3 of Mitchell et al. (2020). To facilitate comparison, we also bin our galaxies by the V_{max} of their host haloes, and predict η_{ceh} from their M_* and $s\text{SFR}$ using the best-fitting model shown in Figure 4. The errorbars are the $1-\sigma$ scatters about the mean. The η_{kin} curves all have inflections at $V_{\text{max}} > 200 \text{ km s}^{-1}$, signalling the takeover by AGN

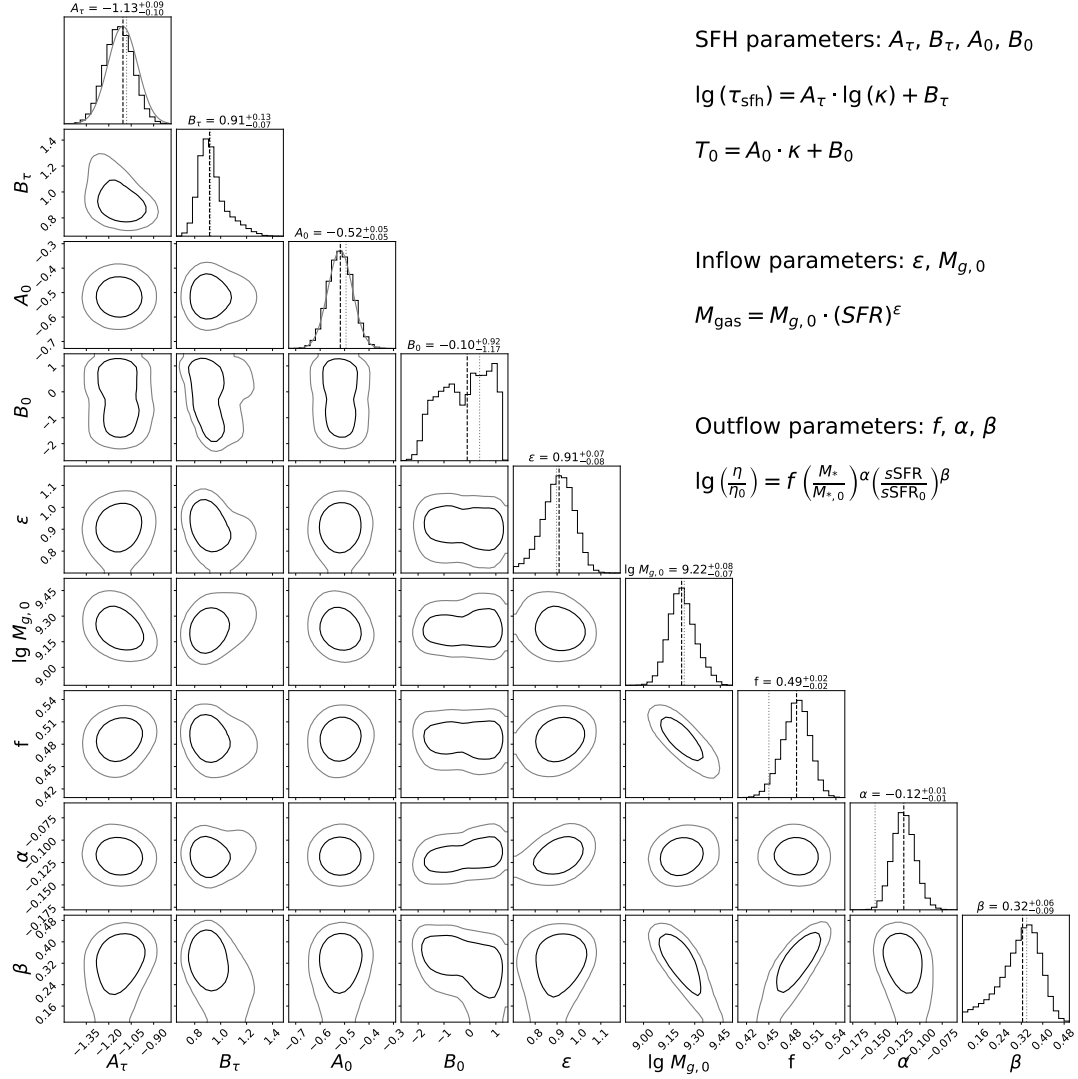


Figure 9. Constraints on the NE-CEM parameters from the mock test of using the $Z_{\text{gas}}(M_*, \dot{M}_*)$ relation of EAGLE galaxies at $z=0.1$ as input data in our Bayesian inference. Contours in the off-diagonal panels indicate the 68% (black) and 95% (gray) confidence regions on the 2D plane that comprised of all the pair sets of nine model parameters (parameter definitions shown in the top right formulae). Histograms in the diagonal panels show the 1D posterior distributions of individual parameters, with gray distributions in the A_τ and A_0 panels representing the Gaussian priors. Dark dashed and light dotted vertical lines in each diagonal panel indicate the parameter value estimated from the 1D posterior mean and that measured directly from the simulation, respectively. The 1σ posterior constraint of each parameter is listed on top of the respective diagonal panel.

feedbacks in more massive galaxies. Below $V_{\text{max}}=200\text{km s}^{-1}$ where stellar feedback dominates, the two types of measurements are generally consistent with each other within the errorbars across all four redshift bins, except for some of the low-mass systems in the highest redshift bin ($V_{\text{max}}<100$). Although the agreement is not perfect, the fact that two entirely different methods, one chemical and the other kinematical, yield mass loading factors that are quantitatively similar, is quite remarkable.

The overall agreement shown in Figure 6 is also very encouraging — our method of parametrising η_{ceh} as a function of M_* and $s\text{SFR}$ in Equation 20 not only appears reasonable from a theoretical perspective, but also predicts the correct scaling of the mass-loading factor with V_{max} and z . In particular, reproducing the correct redshift evolution of η is highly nontrivial. As we emphasized in §2.2.3, η should in principle be determined by the internal state of a galaxy, whose redshift evolution then drives the apparent dependence of η on z . Therefore, this agreement seen in Figure 6 further strengthens

our belief in the physical robustness behind our parametrisation of η , especially when applied to the real observations.

3 A COMPREHENSIVE NON-EQUILIBRIUM CHEMICAL EVOLUTION MODEL

3.1 Assembling the NE-CEM

After developing analytic models for the histories of star formation and mass-loading in the EAGLE simulation, we now assemble a comprehensive NE-CEM for the star-formation main sequence observed at z_{obs} as follows. For an observed $Z_{\text{O}}(M_*^{\text{obs}}, \dot{M}_*^{\text{obs}})$ relation consisting of N galaxy samples within different 2D bins of $(M_*^{\text{obs}}, \dot{M}_*^{\text{obs}})$,

- We describe the average SFH of each sample using Equation 5. For each sample, we solve the value of κ from M_*^{obs} and \dot{M}_*^{obs} via the

inverse function of $\mathcal{F}(\kappa)$ in Equation 6, and then compute τ_{sfr} and t_0 from κ using Equations 3 and 4, respectively. Therefore, the N average SFHs can be predicted with just four parameters $\{A_\tau, B_\tau, A_0, B_0\}$.

- The gas mass $M_{\text{gas}}(t)$ is predicted from SFHs using Equation 13, which requires two parameters $\{M_{g,0}, \epsilon\}$. Note the gas mass M_{gas} in our NE-CEM model is a measure of the effective amount of ISM that has participated in the recycling, mixing, and loading of metal under our one-zone open-box assumption. Therefore, although Equation 13 resembles the observed volumetric star-formation law, we do not expect the slope ϵ to be directly linked to that of the observed star-formation law.

- The mass-loading factors $\eta(t)$ are predicted from $M_*(t)$ and $s\text{SFR}(t)$ from Equation 20 with three parameters $\{f, \alpha, \beta\}$. Finally, the evolution of Z_O can be predicted by numerically integrating Equation 15 for each of the N galaxy samples from t_0 to t_{obs} .

Despite the comprehensiveness of the analytic framework, our full NE-CEM has only nine parameters in total: $\{A_\tau, B_\tau, A_0, B_0, \epsilon, M_{g,0}, f, \alpha, \beta\}$. Among the three steps, the first step can be significantly improved in the future by applying SED fits to the average spectra assuming powexp SFH (Chen et al. *in prep*).

3.2 NE-CEM: features of time-varying τ_* and η

Figure 7 illustrates the impact of different ϵ (left panel) and combinations of (α, β) (right panel) on the trajectory of chemical enrichment for a typical powexp SFH (same as that of the “young” galaxy shown in Figure 3) under our NE-CEM framework. Unsurprisingly, compared to the simple case with constant τ_* and η shown in Figure 3, the full NE-CEM with time-varying τ_* and η exhibits significantly more complex behaviors. In the left panel, we vary the value of ϵ to be 1 (black solid), 1.5 (blue dashed), and 0.7 (red dotted) while keeping other parameters fixed except for f , which we adjust to make the three trajectories arrive at the same Z_O at $z=0$ (star symbol). The equilibrium metallicities and timescales are indicated by the corresponding short horizontal and vertical lines, respectively. The equilibrium timescale is defined as the epoch at which Z_O reaches $(1 - 1/e) = 63.2\%$ that of the equilibrium value. We note that the equilibrium timescales in the NE-CEM differ from $\tilde{\tau}$ (previously defined in Equation 17), which is only valid when both τ_* and η stay constant. For NE-CEM, the equilibrium timescale is determined by the time evolution of η (and also τ_* , but to a lesser degree). The system with $\epsilon=0.7$ does not have an equilibrium metallicity because $dZ_O/dt \rightarrow \epsilon Z_O / \tau_{\text{sfr}} > 0$ (Equation 15) at large t . The inset panel shows the respective evolutions of $M_{\text{gas}}(t)$, with the $\epsilon=1$ curve having exactly the same shape as the SFH because the $M_{\text{gas}}-\dot{M}_*$ scaling is linear. Note that the gas reservoir M_{gas} is not “steady” and varies more than an order of magnitude across the lifetime of the galaxy in all three cases. Similarly, the right panel shows the impact on the CEH caused by the different MLHs due to the change in α and/or β (indicated by the legend in the top left corner), with the inset panel illustrating the variations of η as functions of time.

Comparing the two panels of Figure 7, we find that the impact of ϵ on the CEH is relatively small compared to the that caused by α and β . In particular, the fiducial $\eta(t)$ ($\alpha = -0.12, \beta = 0.35$; black solid curve on the right panel) measured from the EAGLE simulation results in a large equilibrium timescale of 22.4 Gyr, with the metallicity steeply increasing at the current epoch; The CEH predicted using $\alpha=0$ and $\beta=0.35$ (red dotted) experiences a steeper initial rise but a shallower late surge than the fiducial curve, yielding a slightly larger equilibrium timescale of 25.5 Gyr. Thus, both systems with positive β (hence significant time-variation of η ; inset panel) would spend

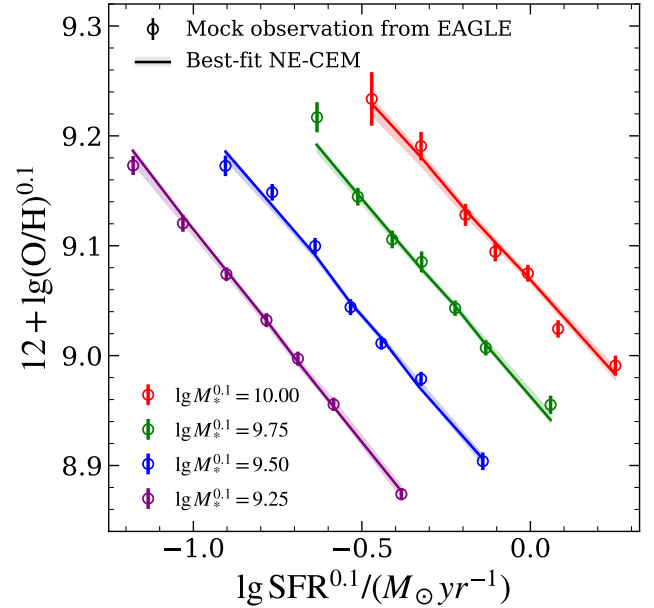


Figure 10. Comparison between the $Z_{\text{gas}}(M_*, \dot{M}_*)$ relation at $z=0.1$ measured directly from EAGLE (open circles with errorbars) and predicted by the posterior mean NE-CEM model (curves with 1σ uncertainty bands). The errorbars on the data points are the standard errors of the mean, while the four colours indicate the four stellar mass bins listed in the bottom left corner.

their past lifetime in a non-equilibrium state, which can only be accurately described by an NE-CEM. In contrast, the other two cases with $\beta=0$ (blue dashed) and constant η (green dot-dashed) experience rapid enrichment at early times and approach chemical equilibrium at 5.6 Gyr and 3.5 Gyr, respectively, well before the current epoch, and therefore can be reasonably described by the standard equilibrium-type CEMs. Comparing the trajectories of the CEH with that of the MLH (inset panel), we can see that the shapes of the histories are strongly correlated, suggesting a potentially tight connection between the slopes of the observed $Z_{\text{gas}}(M_*, \dot{M}_*)$ relation and the slopes of mass-loading — α and β .

Note the asymptotic behaviors at $t \rightarrow +\infty$ shown in Figure 7 depend sensitively on the tail of the SFH. In the real Universe the galaxies would likely be quenched (e.g., also by outflows; Garling et al. 2022) at some large but finite t , i.e., having $\dot{M}_*=0$ and $M_{\text{gas}}=0$, instead of continuing forming stars with an infinitesimal rate. For describing these “red and dead” galaxies, in the future we plan to add a transition from the powexp model to a linear ramp after some quenching timescale, as proposed by Simha et al. (2014).

3.3 Connecting $Z_O(M_*, \dot{M}_*)$ to $\eta_{\text{ceh}}(M_*, s\text{SFR})$

Following the discussion in §3.2, we discover that the average CEH of a galaxy sample depends sensitively on the shape of the mass-loading history, which in turn is determined by the combination of α and β for any given SFH. Therefore, it is of vital importance to ask the following question: how are the slopes of the observed $Z_O(M_*, \dot{M}_*)$ relation, i.e., slope p of the Z_O-M_* relation at fixed \dot{M}_* and slope q of the $Z_O-\dot{M}_*$ relation at fixed M_* , connected to α and β in Equation 20? The key to unlocking the underlying physics of galactic outflows from FMR observations lies in the answer to this question. In the simplest (but unphysical) scenario, if a galaxy is always in chemical

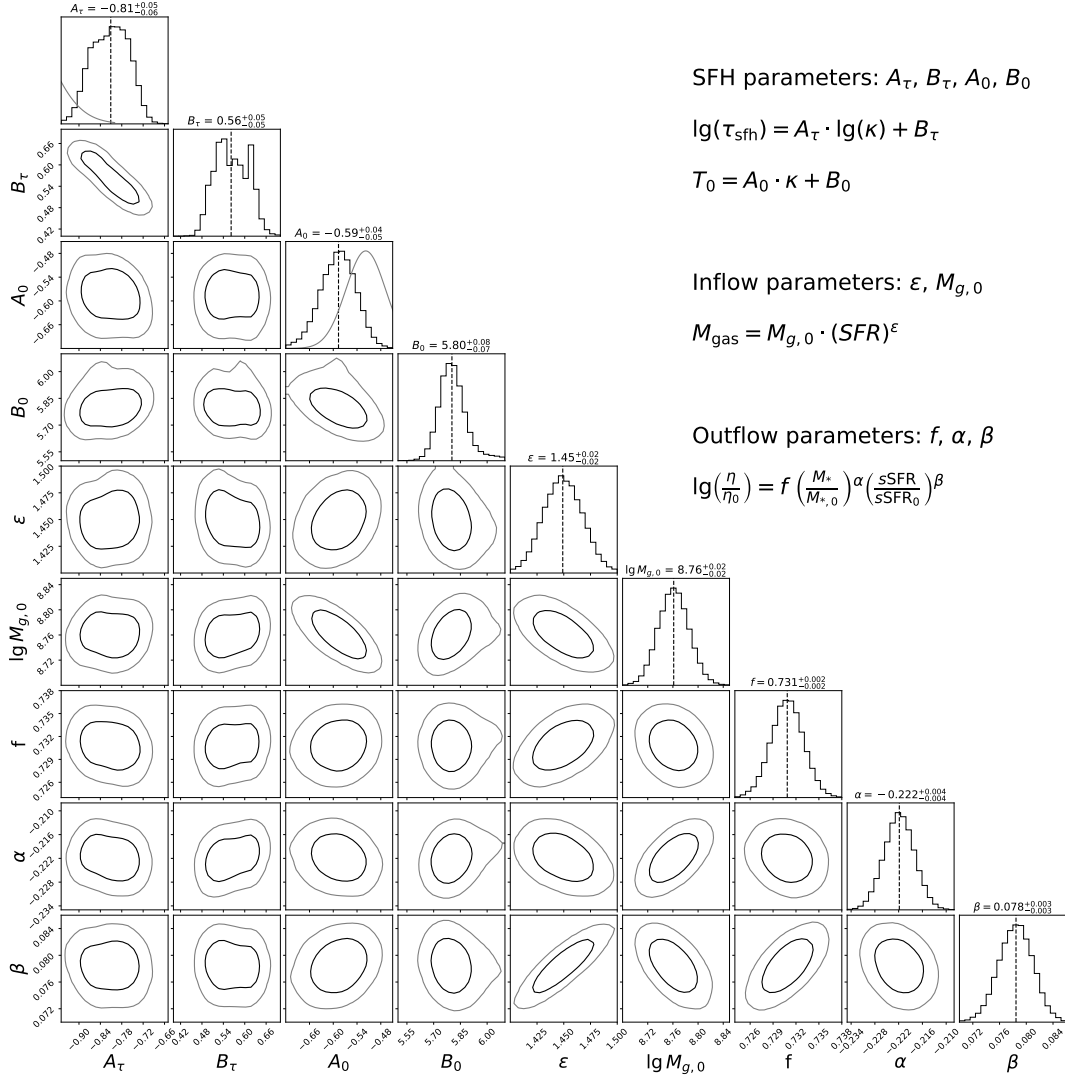


Figure 11. Similar to Fig 9, but for the NE-CEM constraints using the $Z_{\text{gas}}(M_*^{\text{obs}}, M_*^{\text{obs}})$ relation measured from SDSS by Mannucci et al. (2010).

equilibrium, by reaching $Z_{\text{O,eq}}$ instantaneously (i.e., $\tilde{\tau} \ll \tau_*$) at every epoch with changing M_* and $s\text{SFR}$ (hence changing η), its metallicity at that epoch should be connected to its instantaneous mass-loading factor $\eta(M_*, s\text{SFR})$ via

$$Z_{\text{O}}(M_*, \dot{M}_*) \simeq \frac{m_{\text{O}}^{\text{cc}}}{1 + \eta(M_*, s\text{SFR}) - r} \sim \frac{m_{\text{O}}^{\text{cc}}}{\eta(M_*, s\text{SFR})}, \quad (21)$$

from which we expect p and q to depend solely on $\alpha - \beta$ and β , respectively.

To investigate the connection between (p, q) and (α, β) in NE-CEM, we set up an experiment by computing the values of p and q at $\lg \dot{M}_*^{0.1} = -0.5$ and $\lg \dot{M}_*^{0.1} = 9.5$, respectively, on a grid of (α, β) using the fiducial model calibrated against the EAGLE simulation while keeping the seven other parameters fixed. The result of this experiment is displayed in Figure 8, where we show the contours of p and q (contour levels shown in-line) on the α vs. β plane in the top left and bottom left panels, respectively. The four different coloured symbols in each contour panel indicate the loci of the four sets of (α, β) (values in the parentheses by each symbol) that we select to show the predictions of the scaling relations (in matching colours and symbols) on the corresponding right panel.

In the top left panel of Figure 8, the contour lines of constant p are largely aligned in the diagonal direction, i.e., lines of constant $\alpha - \beta$, when $|\alpha|$ and β are both small. This is consistent with the naive expectation from Equation 21, suggesting that outflows are the primary driver of Z_{O} whether it be in or out of equilibrium. In the top right panel, however, although the predicted relations (best-fitting solid lines through large symbols) have slopes increasing from $p=0.39$ (red inverted triangle) to 0.58 (purple square) as $\alpha - \beta$ decreases from -0.3 to -0.7 , they differ substantially between $p=0.46$ (green circles) and $p=0.53$ (blue triangle) despite having the same $\alpha - \beta = -0.5$. In addition, the value of p can be modified by changing ϵ . The two small green circles show the predicted scaling after we increase (dashed line through filled circles) or decrease (dotted line through open circles) the value of ϵ by 0.4 while keeping all other parameters the same as those for the large green circle. Consequently, the value of p increases by 0.03 and decreases by 0.05, respectively. Therefore, the slope in the mass-metallicity relation is largely determined by the stellar mass-dependence of η in the NE-CEM, but is also strongly affected by the $s\text{SFR}$ -dependence of η as well as ϵ , i.e., the \dot{M}_* -dependence of τ_* .

By the same token, the contour lines of constant- q in the bottom

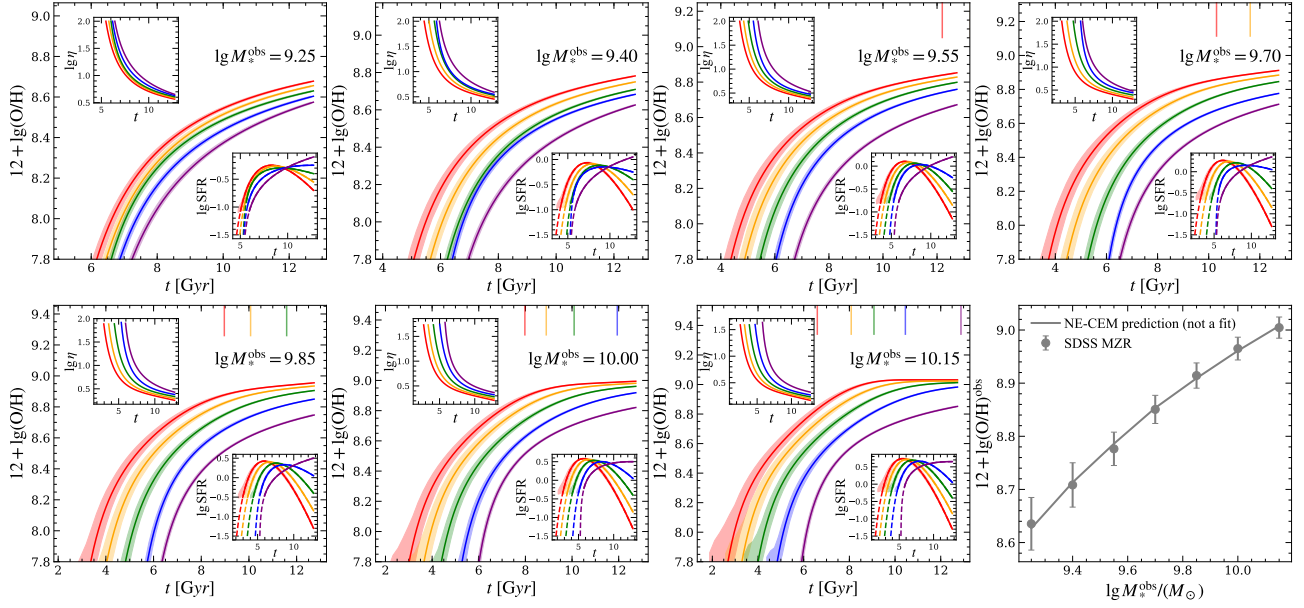


Figure 12. Histories of chemical enrichment (main panels), mass loading (inset panels in the top left corners), and star formation (inset panels in the bottom right corners) predicted by the posterior mean NE-CEM for SDSS galaxies in seven stellar mass bins (with M_*^{obs} increasing from left to right, top to bottom). The bottom rightmost panel shows the average metallicities of the seven M_*^{obs} bins measured from SDSS (gray circles with errorbars) and predicted by the posterior mean NE-CEM (gray curve; not a fit). In each panel of the seven stellar mass bins, we show the predicted CEHs, MLHs, and SFHs along with their respective 1σ uncertainty bands for galaxies in five M_*^{obs} bins. To avoid clutter, we do not show all the M_*^{obs} bins for the high- M_*^{obs} samples. The equilibrium timescale of each CEH is indicated by the short vertical line on the top with matching colour, should it be shorter than the age of the Universe today (increasingly more common with increasing M_*^{obs}). The dashed portions of the SFHs in the inset panels represent the extrapolation before the starting point of each SFH (i.e., epoch at which galaxies accumulated 1% of the final observed mass).

left panel of Figure 8 are mostly horizontal, suggesting the slope of the Z_0 - \dot{M}_* relation is primarily set by β , modulo some residual dependence on α . Similar to the top right panel, the predicted slopes in the bottom right panel confirm the suggestion, with little discrepancy between blue triangles (-0.29) and red inverted triangles (-0.28), nor between green circles (-0.38) and purple squares (-0.38). The ± 0.4 variations in ϵ mostly act to reduce the amplitude of the scaling relation, while making the slope slightly shallower with $\Delta p = -0.03$ and -0.05 , respectively.

To answer the question raised at the beginning of this subsection, Figure 8 demonstrates that for galaxies in the EAGLE simulation, the slope in the mass-metallicity relation at fixed \dot{M}_* is closely linked to $\alpha - \beta$, while the slope in the SFR-metallicity relation at fixed M_* is directly tied to β . Such a tight connection between the two sets of slopes suggests that, despite the galaxies are generally out of equilibrium, our comprehensive NE-CEM could still provide a promising avenue to extracting the underlying physics of galactic outflows from the observed $Z_{\text{gas}}(M_*^{\text{obs}}, \dot{M}_*^{\text{obs}})$ relation.

3.4 Constraining mass loading from gas-phase metallicities: a mock test with EAGLE

To test the feasibility of constraining mass loading from metallicities, we perform a Bayesian inference analysis over the EAGLE simulation data using our comprehensive NE-CEM described in §3.1. We employ a mock data set of the metallicity-stellar mass-SFR relation at $z=0.1$, using the mean oxygen abundances $Z_{\text{O}}^{0.1}$ of the same 28 bins of $(M_*^{0.1}, \dot{M}_*^{0.1})$ as in Figure 2 and 5. In addition, we convert the values of Z_0 to $Z_{\text{gas}} \equiv 12 + \lg(\text{O}/\text{H})$ using $Z_{\text{gas}} = 12 + \lg(Z_0 / (16X_{\text{ISM}}))$, where X_{ISM} is the hydrogen mass fraction in the ISM and we adopt a constant $X_{\text{ISM}} = 0.7$. Therefore, the data vector \mathbf{x} comprises of 28

elements and we adopt the standard errors of the mean as the mock uncertainties of Z_{gas} , i.e., the diagonal errors of the uncertainty matrix \mathbf{C} . We do not consider covariance between different bins and set all the off-diagonal terms of \mathbf{C} to zero.

We predict the oxygen abundances for the 28 bins of $(M_*^{0.1}, \dot{M}_*^{0.1})$ as our model vector $\bar{\mathbf{x}}$ using the NE-CEM with nine model parameters $\theta \equiv \{A_\tau, B_\tau, A_0, B_0, \epsilon, M_{g,0}, f, \alpha, \beta\}$. We assume a Gaussian likelihood model to compute the likelihood distribution of \mathbf{x} given θ

$$p(\mathbf{x}|\theta) \propto \exp\left\{-\frac{1}{2}(\mathbf{x} - \bar{\mathbf{x}})^T \mathbf{C}^{-1}(\mathbf{x} - \bar{\mathbf{x}})\right\}. \quad (22)$$

For the prior distributions, we apply Gaussian priors informed by the EAGLE measurements on $A_\tau \sim \mathcal{N}(-1.11, 0.1^2)$ and $A_0 \sim \mathcal{N}(-0.52, 0.05^2)$, respectively, while adopting flat, uninformative priors on the other parameters.

Given the data vector \mathbf{x} , model vector $\bar{\mathbf{x}}$, and the error matrix \mathbf{C} , the posterior probability is proportional to the product of the likelihood and the prior probability $p(\theta)$

$$p(\theta | \mathbf{x}) \propto p(\mathbf{x}|\theta) p(\theta). \quad (23)$$

For the model inference, we employ the affine invariant Markov Chain Monte Carlo (MCMC) ensemble sampler `emcee` (Foreman-Mackey et al. 2013). We run the MCMC sampler for 3200000 steps for our analysis to ensure its convergence, and derive the posterior constraints after a burn-in period of 240000 steps.

The parameter constraints from our mock test are shown in Figure 9. The histograms in the diagonal panels show the 1D marginalised posterior distributions of each of the nine parameters, and the contours in the off-diagonal panels are the 68% and 95% confidence regions for each of the parameter pairs. In the top right

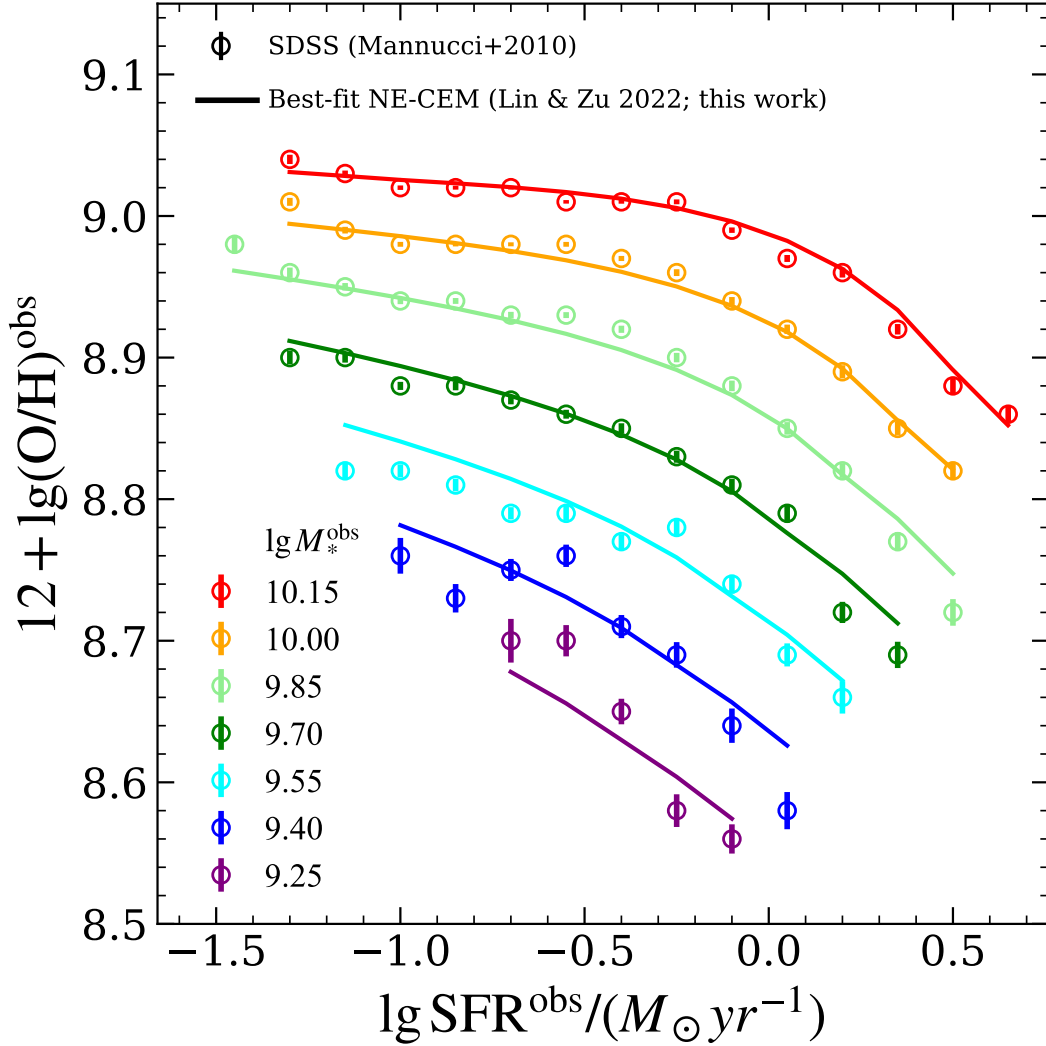


Figure 13. Comparison between the $Z_{\text{gas}}(M_*^{\text{obs}}, \dot{M}_*^{\text{obs}})$ relation measured by Mannucci et al. (2010) from SDSS (circles with errorbars) and that predicted by our posterior mean NE-CEM (curves). Different colours correspond to galaxies in different M_*^{obs} bins, indicated by the legend in the bottom left corner. NE-CEM provides an excellent description of the measurements from SDSS.

corners, we provide a brief description of each model parameter using the relevant equations. The median values and the 68 per cent confidence limits of the 1D posterior constraints are listed on top of each histogram. In each diagonal panel, solid and dashed lines indicate the posterior mean from the Bayesian analysis and the best-fitting value from our calibrations against the EAGLE simulation, respectively. The two sets of best-fits are generally in very good agreement with each other, except for f (0.49 ± 0.02 vs. 0.45 ± 0.01) and α (-0.12 ± 0.02 vs. -0.15 ± 0.02). Naively, one may regard the apparent discrepancies in f and α alarming, but applying the posterior means of $f=0.49$, $\alpha=-0.12$, and $\beta=0.32$ to Equation 20 actually provide a reasonably good fit to the data points in Figure 4, yielding a scatter (0.08 dex) that is only slightly larger than obtained by the direct calibration (0.05 dex). Therefore, our Bayesian inference using the metallicities at $z=0.1$ successfully recover the input parameters that we directly measured from the histories of galaxies in the EAGLE simulation.

Finally, Figure 10 compares the $Z_{\text{gas}}(M_*, \dot{M}_*)$ measured at $z=0.1$ (circles with errorbars) with that predicted by the posterior

mean model (lines with shaded uncertainty bands). Red, green, blue, and purple indicate galaxies with $\lg M_*=10$, 9.75, 9.50, and 9.25, respectively. The posterior mean prediction provides excellent match to the direct measurements from the EAGLE simulation.

4 A FIRST-CUT APPLICATION TO THE SDSS DATA: UNDERSTANDING FMR AND GALACTIC OUTFLOWS

The mock test in §3.4 demonstrates that our nine-parameter NE-CEM is capable of robustly recovering a comprehensive suite of galactic histories, including star formation, chemical enrichment, and more importantly, mass loading, from the $Z_{\text{gas}}(M_*^{\text{obs}}, \dot{M}_*^{\text{obs}})$ relation observed at a fixed epoch. In this Section, we will apply the NE-CEM analysis directly to the SDSS data, in hopes of gaining insights on the nature of FMR and galactic outflows. We emphasize again that a full application of NE-CEM would include a joint SED-fitting of the galaxy spectra, whereas the analysis below is a first-cut application that demonstrates the efficacy of our model in interpreting real observations.

4.1 Inferring mass loading from galaxy metallicities in SDSS

We adopt the $Z_{\text{gas}}(M_*^{\text{obs}}, \dot{M}_*^{\text{obs}})$ measurements listed in the table 1. of [Mannucci et al. \(2010\)](#) as our input data. In particular, We employ seven stellar mass bins centered at $\lg M_*^{\text{obs}}=9.25, 9.40, 9.55, 9.70, 9.85, 10, \text{ and } 10.15$, leaving out the higher mass galaxies that are more likely dominated by AGN feedbacks. For the individual $(M_*^{\text{obs}}, \dot{M}_*^{\text{obs}})$ bins, we only select those with galaxy number counts larger than 100 to ensure robust average metallicity measurements. For the \dot{M}_*^{obs} bins at $\lg M_*=9.25$, we reduce the number count threshold to 70 as the overall number of low-mass galaxies is low. In total, we employ average metallicity measurements for 76 bins in $(M_*^{\text{obs}}, \dot{M}_*^{\text{obs}})$ as the data vector, and adopt the errors on the mean as the measurement uncertainties.

Following the same methodology as in §3.4, we apply our NE-CEM to the 76 data points of the $Z_{\text{gas}}(M_*^{\text{obs}}, \dot{M}_*^{\text{obs}})$ relation. For each bin of fixed M_*^{obs} and \dot{M}_*^{obs} , we start evolving the NE-CEM from $Z_{\text{O}}=10^{-4}$ (i.e., $Z_{\text{gas}}=6.92$) at the epoch when the galaxies have accumulated 1% of their final mass. We have tested that the final state of those galaxies does not vary if we push the starting points to 0.1% of their mass or reduce the initial metallicity by another factor of ten, as the CEHs quickly settle into the correct enrichment trajectories after the galaxies start evolving.

The parameter constraints from SDSS are shown in Figure 11, with exactly the same format as Figure 9. All the parameters are generally well constrained by the SDSS data, but with some prominent differences compared to the EAGLE predictions. Firstly, the constraint on ϵ is 1.45 ± 0.02 , while in EAGLE it is 0.91 ± 0.08 . As pointed out in §3.2, the difference caused by $\epsilon > 1$ vs. < 1 in the CEHs between SDSS and EAGLE galaxies is small, although the two could have distinct paths of enrichment in the future. Secondly, based on the constraints on $\{A_\tau, B_\tau, A_0, B_0\}$, the SDSS data require the galaxies to have rather different SFHs than predicted by EAGLE (e.g., the posterior distribution of A_τ is shifted by 0.32 from the prior), so that younger galaxies started out much later than their older counterparts with the same observed stellar mass. This discrepancy between the EAGLE and SDSS results is largely induced by the differences in the s SFR between the EAGLE predictions and SDSS observations ([Schaye et al. 2015](#)). Lastly, the SDSS data require $\lg \eta$ to scale more strongly with M_* ($\alpha = -0.222 \pm 0.004$) than in EAGLE (-0.12 ± 0.01), but have significantly weaker dependence on s SFR ($\beta = 0.078 \pm 0.003$) than EAGLE (0.32 ± 0.07).

A more visually appealing presentation of our constraints is displayed in Figure 12, where we show the CEHs, MLHs, and SFHs predicted by the posterior mean NE-CEM in the main and two inset panels, respectively (top row and the first three rows in the bottom, with M_*^{obs} increasing from left to right, top to bottom). The shaded bands are the $1-\sigma$ uncertainties, and the dashed portion of the SFHs indicates the histories before the galaxies have gained 1% of their final mass. The SFHs exhibit a clear “downsizing”, i.e., the more massive galaxies started forming stars and enrich their ISM earlier than the less massive ones ([Spitoni et al. 2020](#)). Interestingly, for galaxies with different \dot{M}_*^{obs} in the same M_*^{obs} bin, although the SFHs have drastically different shapes, their star formation (inset panel in the bottom right) conspires with outflows (inset panel in the top left) to produce very coherent CEHs (main panel). In addition, the equilibrium timescales are indicated by the short vertical lines underneath the top x-axis of each panel should they occur before $z=0.1$ — the more massive galaxies are progressively closer to equilibrium, and at the same mass galaxies with lower \dot{M}_*^{obs} are preferentially closer to equilibrium and have older age ([Duarte Puertas et al. 2022](#)). The bottom rightmost panel shows the excellent agreement between the

MZR measured by averaging the observed $Z_{\text{gas}}(M_*^{\text{obs}}, \dot{M}_*^{\text{obs}})$ at each M_*^{obs} (circles with errorbars) and that predicted by the posterior mean NE-CEM (solid curve; not a fit).

Finally, Figure 13 shows the comparison between the $Z_{\text{gas}}(M_*^{\text{obs}}, \dot{M}_*^{\text{obs}})$ relation measured by [Mannucci et al. \(2010\)](#) (circles with errorbars) and predicted by the posterior mean NE-CEM (curves with uncertainty bands), with the colours indicating the observed stellar mass (increasing from purple to red). Overall, the NE-CEM provides excellent fits to the SDSS data points. In particular, the agreement in the high-mass bins, where the observed metallicities exhibit a plateau at the low- \dot{M}_* end but steeply declines at the high- \dot{M}_* end, is highly nontrivial. In the posterior mean NE-CEM, the shallower slope at the low- \dot{M}_* end is caused by the relatively short equilibrium timescale of the massive, almost-quenched galaxies, which have already arrived at the equilibrium metallicities by the time they are observed.

4.2 Can we reproduce the FMR using our non-equilibrium CEM?

The posterior mean NE-CEM obtained in §4.1 not only provides an excellent description of the $Z_{\text{gas}}(M_*^{\text{obs}}, \dot{M}_*^{\text{obs}})$ relation of galaxies observed at $z \sim 0$, but also predicts the entire histories of chemical enrichment for those galaxies, i.e., the $Z_{\text{gas}}(M_*, \dot{M}_* | z)$ relation of their progenitors in the past ($z > 0$). For any successful model of CEM, it is imperative to explain the apparent invariance of the $Z_{\text{gas}}(M_*^{\text{obs}}, \dot{M}_*^{\text{obs}})$ relation with redshift as suggested by the observations (e.g., [Mannucci et al. 2010](#)). With most of the galaxies out of equilibrium, it would be interesting to find out if an FMR still manage to emerge from the progenitor galaxies at $z > 0$.

Figure 14 explores the chemical enrichment of galaxies on the star-formation “phase” diagram (i.e., 2D plane of M_* vs. \dot{M}_*) predicted by the posterior mean NE-CEM (left panel), as well as the resulting 2D map of Z_{gas} on the same diagram (right panel). In the left panel, the rainbow-coloured curves indicate the chemical enrichment (colour gradient) along the star-forming trajectories (curves) of each of the 76 bins of galaxies on the phase diagram, colour-coded by the colourbar on the top left. The star symbols indicate the end points of the trajectories at $z=0$, which correspond to the curves shown in Figure 13 for the six stellar mass bins. As expected, the six bundle of trajectories are self-similar, because galaxies of different masses follow the same powexp family of SFHs. In particular, the trajectory of a more massive galaxy can be obtained by shifting that of a less massive galaxy diagonally to the top right of the phase diagram, i.e., via the rescaling of $\dot{M}_{*,0}$ in Equation 2; Within the same bundle (i.e., the same M_*^{obs}), the trajectories of galaxies with different \dot{M}_*^{obs} are also approximately self-similar by the rescaling of the time variable by their respective τ_{sfr} in Equation 2.

More important, the chemical enrichment along different but self-similar star-forming trajectories appear coherent on the M_* vs. \dot{M}_* diagram in the left panel. This coherence can be qualitatively understood as follows. Take the six most quiescent “galaxies” (i.e., the lowest \dot{M}_*^{obs} curves of each of the six M_*^{obs} bins) for an example, the trajectory of any of the five more massive galaxies (e.g., galaxy B) is approximately a rescaled version of that of the least massive galaxy (galaxy A) by $\mathcal{R} = \dot{M}_{*,0}^B / \dot{M}_{*,0}^A > 1$, which is equivalent to shifting the trajectory diagonally by $\lg \mathcal{R}$ on the log-log diagram. If chemical enrichment is independent of \mathcal{R} and thus retains the perfect self-similarity, the loci of constant Z_{gas} would also appear diagonally on the diagram, producing an FMR in the form of $Z_{\text{gas}} \equiv Z_{\text{gas}}(\mu_x = \lg M_* - x \lg \dot{M}_*)$ with $x=1$. However, the chemical

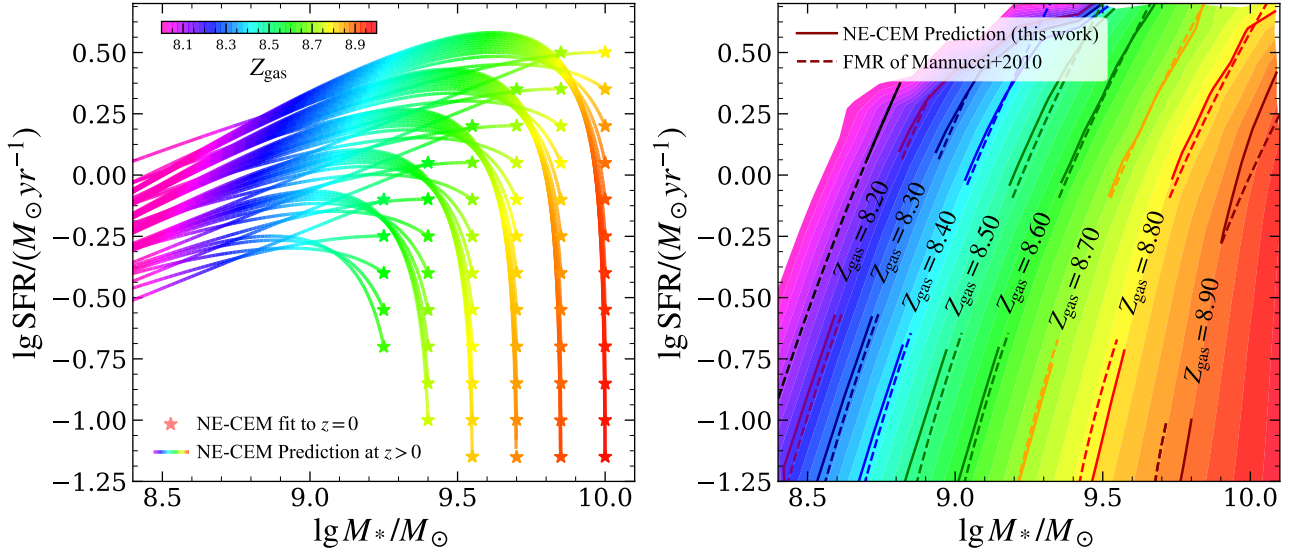


Figure 14. The emergence of a “fundamental metallicity relation” (right panel) from the coherent metal enrichment of different galaxies along their trajectories on the phase diagram of M_* vs. \dot{M}_* (left panel), predicted by our posterior mean NE-CEM. The rainbow colours in both panels indicate the level of metal enrichment, ranging from $Z_{\text{gas}}=8.2$ (purple) to 9.0 (red) as coded by the colourbar in the top left corner of the left panel. *Left panel:* Each individual rainbow-coloured curve corresponds to one of the 76 bins of $(M_*^{\text{obs}}, \dot{M}_*^{\text{obs}})$ (i.e., an average galaxy) in Figure 13, delineating the chemical enrichment of the average galaxy as it evolves from low to high M_* before arriving at the final mass of M_*^{obs} observed by SDSS at $z=0$ (star symbols). *Right panel:* Colour contours with the 2D metallicity map of galaxies on the M_* vs. \dot{M}_* plane, predicted by the posterior mean NE-CEM by populating the phase diagram on the left panel with trajectories of a dense grid of average galaxies. Solid and dashed contour lines represent the FMR predicted from the NE-CEM and that proposed by Mannucci et al. (2010), respectively.

enrichment in NE-CEM is governed by Equation 15, which depends on \mathcal{R} via the dependence of η on M_* and \dot{M}_* in Equation 20. In particular, for two loci (M_*, \dot{M}_*) and $(\mathcal{R}M_*, \mathcal{R}\dot{M}_*)$ on the trajectories of A and B, respectively, the enrichment rate dZ_{O}/dt will be faster at $(\mathcal{R}M_*, \mathcal{R}\dot{M}_*)$ for galaxy B than at (M_*, \dot{M}_*) for galaxy A, due to the smaller mass-loading factor of outflows in the more massive galaxy (as $\eta_B = \eta_A \mathcal{R}^\alpha < \eta_A$ for $\alpha < 0$). Therefore, the chemical enrichment will be lagging behind the self-similarity prediction, thereby making $x < 1$ while staying coherent on the phase diagram.

To find out whether the coherence seen in the left panel of Figure 14 would indeed produce the observed FMR, we employ our posterior mean NE-CEM to predict the SFHs and CEHs for mock galaxies on a dense grid of M_*^{obs} and \dot{M}_*^{obs} , in order to have a full coverage of the phase diagram. We then compute the average Z_{gas} in each state of M_* and \dot{M}_* on the diagram, shown by the 2D map of Z_{gas} on the right panel of Figure 14 and colour-coded by the same colourbar in the left panel. The solid and dashed contour lines indicate the isometallicity contours predicted by the posterior mean NE-CEM and the FMR inferred by Mannucci et al. (2010) (their equation 4 with $x=0.32$), respectively. The two sets of contour lines are largely aligned and overlapping, exhibiting remarkable consistency between the NE-CEM prediction and the observed FMR for all galaxies at $z \geq 0$. Such consistency also confirms our hypothesis in the Introduction that an FMR with the correct $x=0.32$ could emerge out of the coherent histories of metal enrichment between different star-forming galaxies, without the need to impose chemical equilibrium.

Alternatively, Figure 15 shows the enrichment tracks on the Z_{gas} vs. $\mu_{0.32} \equiv \lg M_* - 0.32 \lg \dot{M}_*$ plane of the 76 bins of galaxies, predicted by our posterior mean NE-CEM (rainbow-coloured curves), colour-coded by redshift according to the colourbar on the top left. Gray dots are the data points from Mannucci et al. (2010) (but including those with $M_*^{\text{obs}} > 10^{10.2} M_\odot$), while the black dashed curve

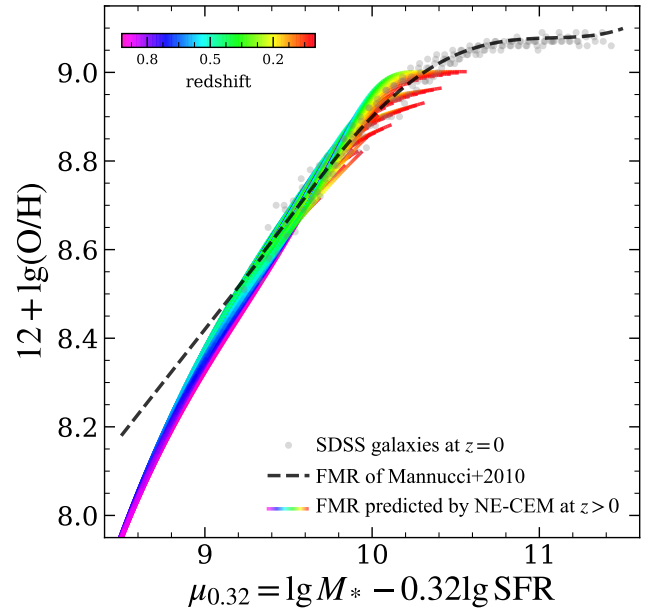


Figure 15. Comparison between the FMR predicted by our posterior mean NE-CEM (coloured curves) and that proposed by Mannucci et al. (2010) (dashed curve). Each rainbow-coloured curve is the predicted track of an average galaxy from one of the 76 bins in Figure 13, colour-coded by the redshifts according to the colourbar on the top left. Gray dots represent the individual measurements from SDSS at $z=0$ by Mannucci et al. (2010), including massive galaxies ($M_*^{\text{obs}} > 10^{10.2} M_\odot$) dominated by AGN feedbacks.

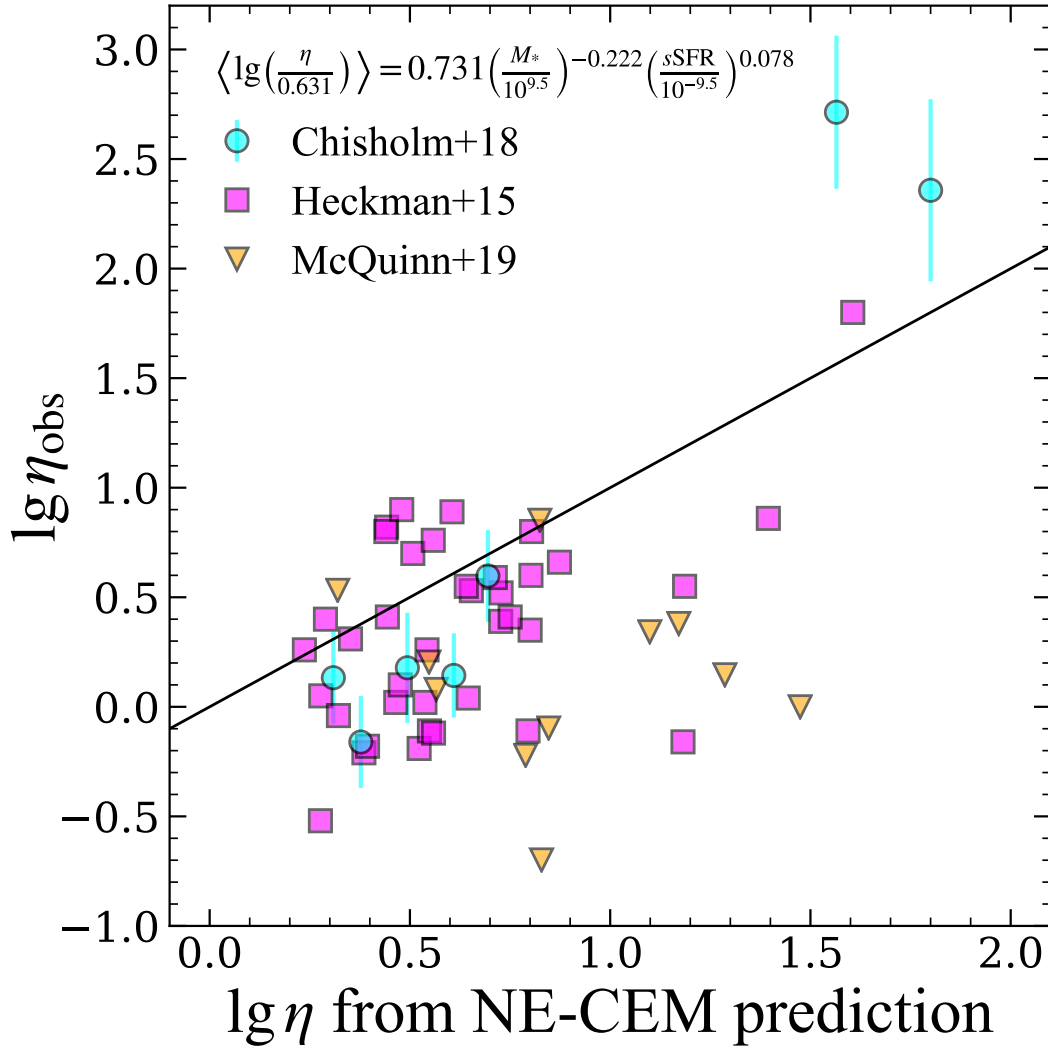


Figure 16. Comparison between the observed mass loading factors (y-axis) and the predictions by our posterior mean NE-CEM from the observed M_* and $s\text{SFR}$ of those galaxies (x-axis) using Equation 24 (also shown in the top left corner). Cyan circles with errorbars, magenta squares, and orange triangles are the measurements from Chisholm et al. (2018), Heckman et al. (2015), and McQuinn et al. (2019), respectively, with the solid straight line indicating the one-to-one relation.

indicates the best-fitting FMR by Mannucci et al. (2010). Our predicted tracks closely follow Mannucci et al.’s best-fit at $\mu_{0.32} > 9$, but drop more steeply with decreasing $\mu_{0.32}$ below $\mu_{0.32} = 9$. Future metallicity observations for a large sample of dwarf galaxies at high redshifts could help test our predicted deviation from the SDSS extrapolation from L_* galaxies. In addition, the scatter between different predicted tracks is consistent with the small scatter in the SDSS FMR inferred by Mannucci et al. (2010) (0.05 dex). This consistency is not only a powerful validation of the success of our NE-CEM framework, but also naturally explains the origin of the tightness of the FMR — star-forming galaxies in the Universe make stars, drive winds, and enrich gas in non-equilibrium yet strikingly coherent fashion.

To answer the question raised by the title of this subsection, the chemical enrichment of galaxies predicted by our NE-CEM at $z > 0$ exhibit excellent consistency with the $z=0$ FMR proposed by Mannucci et al. (2010), thereby successfully reproducing the redshift invariance of the FMR without resorting to equilibrium. We emphasize again that the rainbow curves and contours in Figure 14 and

Figure 15) are *not* direct fits to the FMR proposed by Mannucci et al. (2010), but enrichment trajectories *predicted* by the NE-CEM at $z > 0$. This is non-trivial because unlike the equilibrium models, the progenitors of the current-day galaxies at $z > 0$ may not obey the same $Z_{\text{gas}}(M_*^{\text{obs}}, \dot{M}_*^{\text{obs}})$ relation observed at $z=0$ when assuming non-equilibrium.

4.3 Physical implication of our constraints on η and comparison with direct observations

Our posterior mean mass-loading factor of galactic outflows (assuming entirely entrained ISM) is²

$$\lg\left(\frac{\eta}{0.631}\right) = 0.731 \left(\frac{M_*}{10^{9.5} M_\odot}\right)^{-0.222} \left(\frac{s\text{SFR}}{10^{-9.5} \text{yr}^{-1}}\right)^{0.078}. \quad (24)$$

² This is equivalent to a constraint on the metal-loading factor ζ if the outflows are over-enriched with ISM entrainment fraction below unity. See Equation 8.

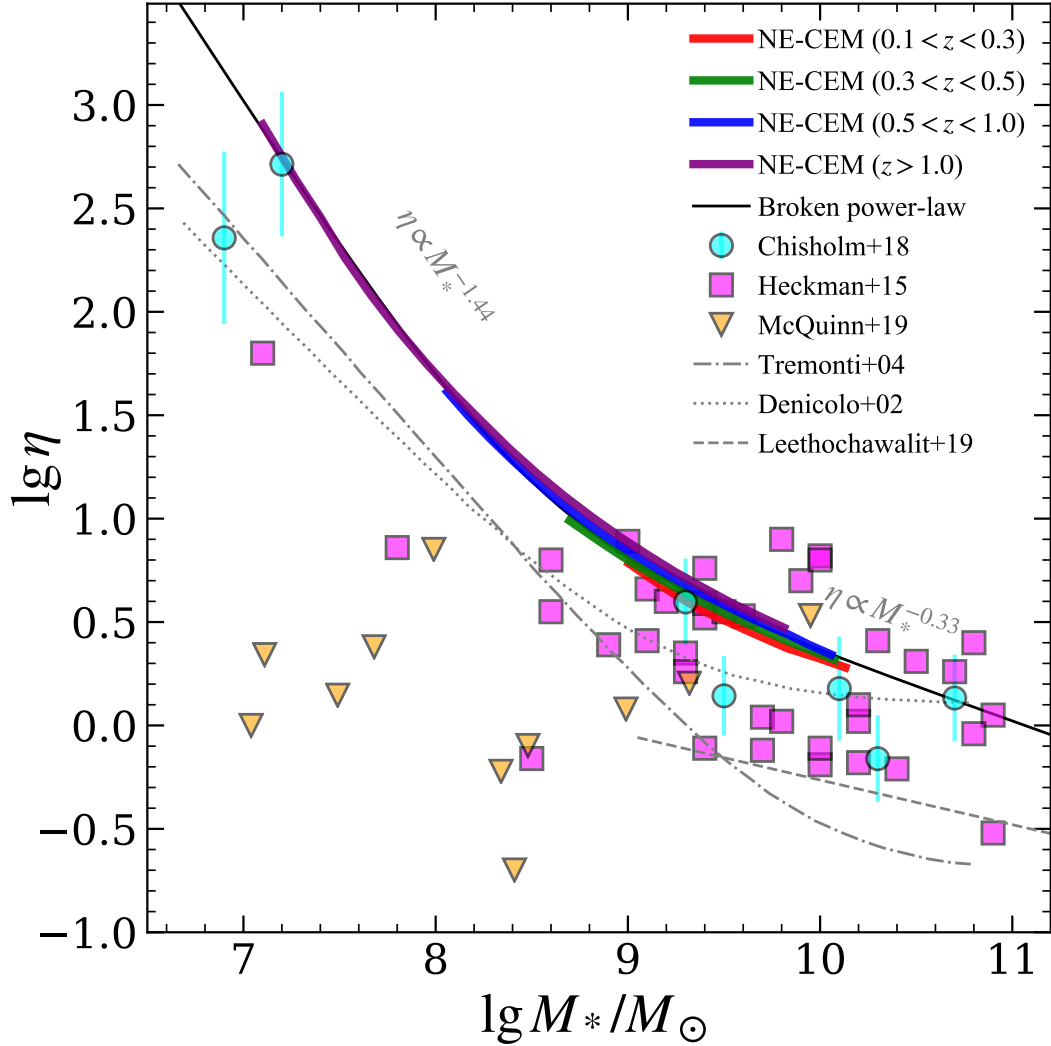


Figure 17. Comparison between the stellar mass-dependence of the mass loading factor inferred from our NE-CEM constraint (thick solid curves) and that from observational measurements (symbols) as well as other empirical constraints (gray curves). We convert our constraint in Equation 24 to an dependence of η on M_* at different z by marginalising over the dependence on $s\text{SFR}$, yielding four $Z_{\text{gas}}-M_*$ relations at $0.1 < z < 0.3$ (thick red curve), $0.3 < z < 0.5$ (thick green), $0.5 < z < 1.0$ (thick blue), and $z > 1.0$ (thick purple). Solid black curve is a broken power-law fit (Equation 25) to the four relations, with $\eta \propto M_*^{-1.1}$ and $\eta \propto M_*^{-0.33}$ at the low- and high-mass ends, respectively. Cyan circles with errorbars, magenta squares, and orange triangles indicate the direct measurements (same as in Figure 16) from Chisholm et al. (2018), Heckman et al. (2015), and McQuinn et al. (2019), respectively. Dashed curve represents the empirical constraint from Leethochawalit et al. (2019), whereas dotted and dot-dashed curves indicate the η - M_* relations inferred by Peeples & Shankar (2011) using the MZR measured by Denicoló et al. (2002) and Tremonti et al. (2004), respectively.

While the anti-correlation between η and M_* is generally expected by various galaxy formation models, the dependence of η on $s\text{SFR}$ or \dot{M}_* is still under debate. For instance, using a high-resolution hydrodynamical simulation of an isolated magnetised Milky Way-like disc galaxy, Wibking & Krumholz (2022) obtained a positive linear correlation between η and \dot{M}_* , and found that the predicted η is indistinguishable from a non-magnetic simulation if the SFH is controlled. However, using a suite of hydrodynamic cosmological zoom-in simulations with an explicit stellar feedback model, Muratov et al. (2015) predicted that η is independent of \dot{M}_* . More intriguingly, using a suite of parsec-resolution local galactic disk simulations with explicit modelling of the ISM, Kim et al. (2020) predicted that the mass-loading factors of the cool gas outflows decrease steeply with the surface density of star formation of different model galaxies, albeit with strong variation in the initial gas surface density.

We detect a weakly positive but statistically significant correlation between η and $s\text{SFR}$ ($\beta=0.078 \pm 0.003$). To further test the necessity of having a non-zero β in our mass-loading model, we repeat the MCMC analysis of §4.1 while fixing the value of β to be zero, and find that such a model is incapable of reproducing the observed $Z_{\text{gas}}(M_*^{\text{obs}}, \dot{M}_*^{\text{obs}})$ relation at $z=0$. Therefore, our NE-CEM analysis makes a strong observational argument for the existence of a positive correlation between η and $s\text{SFR}$ at fixed M_* .

Figure 16 compares the observed mass-loading factors of three sample of galaxies with the predictions by our posterior mean NE-CEM (Equation 24). From the outflowing warm ionized gas traced by ultraviolet (UV) metal absorption lines in low-redshift starburst galaxies ($M_* \sim 10^{7.5} - 10^{11} M_\odot$), Heckman et al. (2015) found the galactic winds travelling at velocities $\sim 100 - 500 \text{ km s}^{-1}$ with an average total column density around 10^{21} cm^{-2} . By assuming isotropic

winds at twice the starburst radii, they estimated the mass-loading factors to be $\eta \sim 1-10$, with weak anti-correlations with M_* or \dot{M}_* . However, our predictions of η from the observed M_* and \dot{M}_* are in excellent agreement with the measurements by Heckman et al. (2015, magenta squares).

Using similar UV observations but very different modelling assumptions, Chisholm et al. (2018) found that the outflows are highly enriched compared to the ISM and the metal-loading factors exhibit strong anti-correction with M_* (cyan circles with errorbars). From H α narrowband deep imaging, McQuinn et al. (2019) estimated the mass-loading factors to be 0.2–7 for a dozen near-by dwarf galaxies with $M_* \sim 10^7-10^{9.3} M_\odot$, but found little dependence of η on M_* or \dot{M}_* (orange triangles). Our NE-CEM constraint agrees reasonably well with both the Chisholm et al. and McQuinn et al. measurements in the $\eta < 10$ regime (i.e., galaxies with $M_* > 10^9 M_\odot$). In the high- η regime occupied by the dwarf galaxies, our constraint slightly under-predicts η for the two dwarf galaxies in Chisholm et al., but over-predicts η for the four low-mass galaxies in McQuinn et al. However, since the two sets of measurements are not consistent with each other for the low-mass systems, more observations of the outflows in the dwarf galaxies are needed to test the predictions from our NE-CEM constraint.

To facilitate the comparison with other empirical constraints of the dependence of mass-loading factors on stellar mass, we convert our constraint on η as in Equation 24 (i.e., as a function of M_* and $s\text{SFR}$) to that on the relations between η and M_* at different redshifts, using the SFHs predicted by the posterior mean NE-CEM. The result is shown in Figure 17, where we compare the stellar mass dependences of the η predicted by our posterior mean NE-CEM at $0.1 < z < 0.3$ (thick red curve), $0.3 < z < 0.5$ (thick green), $0.5 < z < 1.0$ (thick blue), and $z > 1$ (thick purple) with a suite of empirical constraints (thin curves) and observational results (symbols; same as those in Figure 16) from the literature. The four coloured curves exhibit a steeper trend with M_* at the low mass than at the high mass end, which can be described by a broken power-law that scales as $M_*^{-1.44}$ and $M_*^{-0.33}$ at the low and high-mass ends, respectively. In particular, the solid black curve in Figure 17 is

$$\eta = 7 \left(1 + \frac{M_*}{10^{8.5} M_\odot} \right)^{1.10} \left(\frac{M_*}{10^{8.5} M_\odot} \right)^{-1.44}. \quad (25)$$

Note that Equation 25 expresses η as a function of M_* after marginalising over the dependences on $s\text{SFR}$, whereas in our full constraint (Equation 24) η scales as $M_*^{-0.222}$ at any given $s\text{SFR}$.

As expected from Figure 16, our constraint on η (thick coloured curves) and its extrapolation to both higher and lower mass ranges (solid black curve) exhibit a broad agreement with the direct measurements (symbols). Our constraint is slightly higher than the empirical constraints from Peeples & Shankar (2011) using the MZR derived in Tremonti et al. (2004, dot-dashed curve) and Denicoló et al. (2002, dotted curve), as well as the constraint from the Mg abundances of quiescent galaxies in massive clusters (Leethochawalit et al. 2019, dashed curve). The discrepancy is probably due to the different model assumptions on equilibrium and mass-loading, but some of it can be at least partially explained by the different metallicity calibrations in the data (Kewley & Ellison 2008).

5 CONCLUSION

In this paper, we have developed a comprehensive framework of non-equilibrium chemical evolution model (NE-CEM) by explicitly

tracking the average star-formation history of galaxies and the mass-loading history of stellar feedback-driven outflows along the SFH. After exploring the SFHs of galaxies in the EAGLE hydrodynamical simulation, we discover that a simple yet flexible model (powexp) can accurately describe the SFHs of the simulated galaxies, thereby allowing us to robustly reconstruct the average SFHs for the observed galaxies at fixed M_*^{obs} and \dot{M}_*^{obs} .

To explore the parametrisation of the mass-loading factor η , we firstly develop a novel method to reconstruct the evolution of η from the chemical enrichment history of galaxies in hydrodynamical simulations. After applying the reconstruction method to the EAGLE simulation, we discover that the mass-loading at any epoch can be accurately (with a scatter of 0.05 dex) described by the stellar mass M_* and specific star formation rate $s\text{SFR}$ of galaxies at that epoch, so that $\lg \eta \propto M_*^\alpha s\text{SFR}^\beta$ (with $\alpha = -0.15$ and $\beta = 0.34$ in EAGLE). Encouragingly, our chemically-inferred mass-loading factors exhibit remarkable agreement with those measured kinematically by Mitchell et al. (2020) from tracking wind particles in the EAGLE simulation. Such an agreement is highly nontrivial, and since the Mitchell et al. measurement is somewhat analogous to the down-the-barrel measurements of η in the real observations, the agreement greatly reinforces our belief that we can potentially constrain wind kinematics and energetics by applying our NE-CEM method to the real data.

By tracking the chemical enrichment of ISM along the powexp SFH with time-dependent mass-loading of outflows, we can predict the metallicity-stellar mass-SFR relation of the entire star-formation main-sequence at any observed epoch, $Z_{\text{gas}}(M_*^{\text{obs}}, \dot{M}_*^{\text{obs}})$, without the need to assume some equilibrium. The gas accretion history is implicitly tracked via the modelling of the gas reservoir as $M_{\text{gas}} \propto \dot{M}_*^\xi$. Despite the comprehensive predictive power, our NE-CEM has only nine parameters in total. We demonstrate the efficacy of the NE-CEM framework in constraining the mass-loading properties of galactic outflows, i.e., α and β , by performing extensive analytic and mock tests using the $Z_{\text{gas}}(M_*^{\text{obs}}, \dot{M}_*^{\text{obs}})$ measured from EAGLE at $z=0.1$.

As a first-cut application of our NE-CEM framework, we perform a Bayesian inference analysis using the SDSS $Z_{\text{gas}}(M_*^{\text{obs}}, \dot{M}_*^{\text{obs}})$ relation measured by Mannucci et al. (2010). The posterior mean NE-CEM not only provides excellent description of the SDSS $Z_{\text{gas}}(M_*^{\text{obs}}, \dot{M}_*^{\text{obs}})$ relation at $z=0$, but also correctly predicts the redshift invariance of the so-called “fundamental metallicity relation”, $Z_{\text{gas}}(\mu_{0.32})$, with most galaxies far from equilibrium. Therefore, equilibrium or a steady gas reservoir is not a prerequisite for the existence of a fundamental metallicity relation. In our NE-CEM framework, the $Z_{\text{gas}}(\mu_{0.32})$ relation emerges out of the coherent histories of chemical evolution between different star-forming galaxies, due to the self-similarity in their star-forming and mass-loading behaviors.

We obtain a tight constraint on the mass-loading factors from SDSS as

$$\lg \left(\frac{\eta}{0.631} \right) = 0.731 \pm 0.002 \left(\frac{M_*}{10^{9.5}} \right)^{-0.222 \pm 0.004} \left(\frac{s\text{SFR}}{10^{-9.5}} \right)^{0.078 \pm 0.003}, \quad (26)$$

after marginalising over the nuisance parameters (e.g., ϵ) in the NE-CEM. This constraint is broadly consistent with various direct observations and empirical constraints from the literature. In particular, using the observed stellar mass and SFRs of a sample of galaxies in the local Universe, we predict their mass-loading factors and find good agreement with the down-the-barrel observations (e.g.,

Heckman et al. 2015; Chisholm et al. 2018). In addition, the posterior mean NE-CEM predicts that the mass loading factor scales as $\eta \propto M_*^{-1.44}$ and $M_*^{-0.33}$ at the low- and high- M_* ends, respectively, after marginalising over the s SFR dependence. This broken power-law behavior of η is in reasonable agreement with other empirical constraints from the mass-metallicity relation (Peeples & Shankar 2011).

Therefore, our constraint on η provides an excellent benchmark for different sub-grid models of stellar feedbacks in hydrodynamical simulations and SAMs. Despite the increasing sophistication in the explicit modelling of galactic winds in modern cosmological hydrodynamical simulations (Khandai et al. 2015; Schaye et al. 2015; Pillepich et al. 2018; Hopkins et al. 2018; Davé et al. 2019; Vogelsberger et al. 2020; Pakmor et al. 2022), the effective mass-loading of the simulated outflows on galactic scales should be roughly consistent with our constraint, so as to reproduce the correct $Z_{\text{gas}}(M_*^{\text{obs}}, \dot{M}_*^{\text{obs}})$ relations observed between $z=0$ and $z=2.5$.

Looking to the future, our method can be significantly improved in several important aspects. The average SFHs can be more accurately inferred from the stacked spectra of star-forming galaxies at fixed M_*^{obs} and \dot{M}_*^{obs} , by adopting the powexp SFH model (or some modified variant; see e.g., Simha et al. 2014) during SED fitting. By the same token, the average gaseous metallicities can be measured more robustly using the direct method from auroral lines (Andrews & Martini 2013) or self-consistently from the overall SED fitting (Thorne et al. 2022). With upcoming spectroscopic surveys like the DESI (Abareshi et al. 2022) and PFS (Takada et al. 2014), we expect our NE-CEM framework to provide a promising avenue to unlocking the exquisite yet coherent histories of chemical enrichment and stellar feedback in star-forming galaxies across cosmic time.

DATA AVAILABILITY

The data underlying this article will be shared on reasonable request to the corresponding author.

ACKNOWLEDGEMENTS

This article is dedicated to the memory of Dr. Yu Gao, from whom the authors benefited tremendously discussing about the star formation law and gas reservoirs at Xiamen University. We are indebted to David Weinberg for his invaluable suggestions that have greatly improved the overall quality of the paper. We also thank the referee for the helpful comments and Junde Chen for stimulating discussions at the early stage of this work. Y.L. and Y.Z. acknowledge the support by the National Key Basic Research and Development Program of China (No. 2018YFA0404504), the National Science Foundation of China (12173024, 11621303, 11890692, 11873038), the science research grants from the China Manned Space Project (No. CMS-CSST-2021-A01, CMS-CSST-2021-A02, CMS-CSST-2021-B01), and the “111” project of the Ministry of Education under grant No. B20019. Y.Z. acknowledges the generous sponsorship from Yangyang Development Fund, and thanks Cathy Huang for her hospitality during the pandemic at the Zhangjiang Hi-Technology Park where he worked on this project.

REFERENCES

- Abareshi B., et al., 2022, *AJ*, 164, 207
 Andrews B. H., Martini P., 2013, *ApJ*, 765, 140

- Andrews B. H., Weinberg D. H., Schönrich R., Johnson J. A., 2017, *ApJ*, 835, 224
 Barrera-Ballesteros J. K., Sánchez S. F., Heckman T., Blanc G. A., MaNGA Team 2017, *ApJ*, 844, 80
 Bothwell M. S., Maiolino R., Peng Y., Ciccone C., Griffith H., Wagg J., 2016, *MNRAS*, 455, 1156
 Bouché N., et al., 2010, *ApJ*, 718, 1001
 Broussard A., et al., 2019, *ApJ*, 873, 74
 Brown T., Cortese L., Catinella B., Kilborn V., 2018, *MNRAS*, 473, 1868
 Chen X., Wang J., Kong X., 2022, *ApJ*, 933, 39
 Chevalier R. A., Clegg A. W., 1985, *Nature*, 317, 44
 Chisholm J., Tremonti Christy A., Leitherer C., Chen Y., 2016, *MNRAS*, 463, 541
 Chisholm J., Tremonti C., Leitherer C., 2018, *MNRAS*, 481, 1690
 Conroy C., 2013, *ARA&A*, 51, 393
 Crain R. A., et al., 2015, *MNRAS*, 450, 1937
 Cresci G., Mannucci F., Curti M., 2019, *A&A*, 627, A42
 Dalcanton J. J., 2007, *ApJ*, 658, 941
 Dalla Vecchia C., Schaye J., 2012, *MNRAS*, 426, 140
 Davé R., Finlator K., Oppenheimer B. D., 2012, *MNRAS*, 421, 98
 Davé R., Anglés-Alcázar D., Narayanan D., Li Q., Rafieferantsoa M. H., Appleby S., 2019, *MNRAS*, 486, 2827
 Dayal P., Ferrara A., Dunlop J. S., 2013, *MNRAS*, 430, 2891
 De Rossi M. E., Bower R. G., Font A. S., Schaye J., Theuns T., 2017, *MNRAS*, 472, 3354
 Dekel A., Silk J., 1986, *ApJ*, 303, 39
 Denicoló G., Terlevich R., Terlevich E., 2002, *MNRAS*, 330, 69
 Duarte Puertas S., Vilchez J. M., Iglesias-Páramo J., Mollá M., Pérez-Montero E., Kehrig C., Pilyugin L. S., Zinchenko I. A., 2022, *A&A*, 666, A186
 Ellison S. L., Patton D. R., Simard L., McConnachie A. W., 2008, *ApJ*, 672, L107
 Erb D. K., Shapley A. E., Pettini M., Steidel C. C., Reddy N. A., Adelberger K. L., 2006, *ApJ*, 644, 813
 Fielding D., Quataert E., Martizzi D., 2018, *MNRAS*, 481, 3325
 Finlator K., Davé R., 2008, *MNRAS*, 385, 2181
 Forbes J. C., Krumholz M. R., Burkert A., Dekel A., 2014, *MNRAS*, 443, 168
 Foreman-Mackey D., Hogg D. W., Lang D., Goodman J., 2013, *PASP*, 125, 306
 Furlong M., et al., 2015, *MNRAS*, 450, 4486
 Gao Y., et al., 2018, *ApJ*, 869, 15
 Garling C. T., Peter A. H. G., Spekkens K., Sand D. J., Hargis J., Crnojević D., Carlin J. L., 2022, arXiv e-prints, p. arXiv:2209.09262
 Gentry E. S., Krumholz M. R., Dekel A., Madau P., 2017, *MNRAS*, 465, 2471
 Gentry E. S., Krumholz M. R., Madau P., Lupi A., 2019, *MNRAS*, 483, 3647
 Griffith E. J., Sukhbold T., Weinberg D. H., Johnson J. A., Johnson J. W., Vincenzo F., 2021, *ApJ*, 921, 73
 Harwit M., Brisbin D., 2015, *ApJ*, 800, 91
 Heckman T. M., Armus L., Miley G. K., 1990, *ApJS*, 74, 833
 Heckman T. M., Alexandroff R. M., Borthakur S., Overzier R., Leitherer C., 2015, *ApJ*, 809, 147
 Henry A., et al., 2013, *ApJ*, 776, L27
 Hopkins P. F., et al., 2018, *MNRAS*, 480, 800
 Huang Y.-H., Chen H.-W., Johnson S. D., Weiner B. J., 2016, *MNRAS*, 455, 1713
 Huang C., et al., 2019, *ApJ*, 886, 31
 Hughes T. M., Cortese L., Boselli A., Gavazzi G., Davies J. I., 2013, *A&A*, 550, A115
 Hunt L., Dayal P., Magrini L., Ferrara A., 2016, *MNRAS*, 463, 2020
 Iyer K. G., et al., 2020, *MNRAS*, 498, 430
 Iyer K. G., Speagle J. S., Caplar N., Forbes J. C., Gawiser E., Leja J., Tacchella S., 2022, arXiv e-prints, p. arXiv:2208.05938
 Johnson J. A., 2019, *Science*, 363, 474
 Johnson J. W., Weinberg D. H., 2020, *MNRAS*, 498, 1364
 Kacprzak G. G., et al., 2016, *ApJ*, 826, L11
 Katsianis A., Yang X., Zheng X., 2021, *The Astrophysical Journal*, 919, 88
 Kauffmann G., et al., 2003, *MNRAS*, 341, 33

- Kennicutt Robert C. J., 1998, *ApJ*, 498, 541
- Kewley L. J., Ellison S. L., 2008, *ApJ*, 681, 1183
- Khandai N., Di Matteo T., Croft R., Wilkins S., Feng Y., Tucker E., DeGraf C., Liu M.-S., 2015, *MNRAS*, 450, 1349
- Kim C.-G., Ostriker E. C., Raileanu R., 2017, *ApJ*, 834, 25
- Kim C.-G., et al., 2020, *ApJ*, 900, 61
- Koo B.-C., McKee C. F., 1992, *ApJ*, 388, 93
- Lara-López M. A., et al., 2010, *A&A*, 521, L53
- Larson R. B., 1972, *Nature Physical Science*, 236, 7
- Leethochawalit N., Kirby E. N., Ellis R. S., Moran S. M., Treu T., 2019, *ApJ*, 885, 100
- Leja J., Carnall A. C., Johnson B. D., Conroy C., Speagle J. S., 2019, *ApJ*, 876, 3
- Lequeux J., Peimbert M., Rayo J. F., Serrano A., Torres-Peimbert S., 1979, *A&A*, 80, 155
- Li M., et al., 2022, arXiv e-prints, p. arXiv:2211.01382
- Lilly S. J., Carollo C. M., Pipino A., Renzini A., Peng Y., 2013, *ApJ*, 772, 119
- Ly C., Malkan M. A., Rigby J. R., Nagao T., 2016, *ApJ*, 828, 67
- Mac Low M.-M., Ferrara A., 1999, *ApJ*, 513, 142
- Maiolino R., Mannucci F., 2019, *A&ARv*, 27, 3
- Maiolino R., et al., 2008, *A&A*, 488, 463
- Mannucci F., et al., 2009, *MNRAS*, 398, 1915
- Mannucci F., Cresci G., Maiolino R., Marconi A., Gnerucci A., 2010, *MNRAS*, 408, 2115
- McQuinn K. B. W., van Zee L., Skillman E. D., 2019, *ApJ*, 886, 74
- Ménard B., Scranton R., Fukugita M., Richards G., 2010, *MNRAS*, 405, 1025
- Mitchell P. D., Schaye J., Bower R. G., Crain R. A., 2020, *MNRAS*, 494, 3971
- Muratov A. L., Kereš D., Faucher-Giguère C.-A., Hopkins P. F., Quataert E., Murray N., 2015, *MNRAS*, 454, 2691
- Murray N., Quataert E., Thompson T. A., 2005, *ApJ*, 618, 569
- Murray N., Martin C. L., Quataert E., Thompson T. A., 2007, *ApJ*, 660, 211
- Murray N., Ménard B., Thompson T. A., 2011, *ApJ*, 735, 66
- Naab T., Ostriker J. P., 2017, *ARA&A*, 55, 59
- Pakmor R., et al., 2022, arXiv e-prints, p. arXiv:2210.10060
- Peeples M. S., Shankar F., 2011, *MNRAS*, 417, 2962
- Peeples M. S., Werk J. K., Tumlinson J., Oppenheimer B. D., Prochaska J. X., Katz N., Weinberg D. H., 2014, *ApJ*, 786, 54
- Pillepich A., et al., 2018, *MNRAS*, 473, 4077
- Rupke D., 2018, *Galaxies*, 6, 138
- Sánchez S. F., et al., 2013, *A&A*, 554, A58
- Sanders R. L., et al., 2021, *ApJ*, 914, 19
- Savaglio S., et al., 2005, *ApJ*, 635, 260
- Schaye J., Dalla Vecchia C., 2008, *MNRAS*, 383, 1210
- Schaye J., et al., 2015, *MNRAS*, 446, 521
- Schmidt M., 1959, *ApJ*, 129, 243
- Simha V., Weinberg D. H., Conroy C., Dave R., Fardal M., Katz N., Oppenheimer B. D., 2014, arXiv e-prints, p. arXiv:1404.0402
- Somerville R. S., Davé R., 2015, *ARA&A*, 53, 51
- Spitoni E., Calura F., Mignoli M., Gilli R., Silva Aguirre V., Gallazzi A., 2020, *A&A*, 642, A113
- Tacchella S., Forbes J. C., Caplar N., 2020, *MNRAS*, 497, 698
- Takada M., et al., 2014, *PASJ*, 66, R1
- Thorne J. E., et al., 2022, *MNRAS*,
- Tinsley B. M., 1980, *Fundamentals Cosmic Phys.*, 5, 287
- Topping M. W., et al., 2021, *MNRAS*, 506, 1237
- Tremonti C. A., et al., 2004, *ApJ*, 613, 898
- Tumlinson J., Peeples M. S., Werk J. K., 2017, *ARA&A*, 55, 389
- Vasiliev E. O., Shchekinov Y. A., Nath B. B., 2017, *MNRAS*, 468, 2757
- Veilleux S., Cecil G., Bland-Hawthorn J., 2005, *ARA&A*, 43, 769
- Vincenzo F., Matteucci F., Belfiore F., Maiolino R., 2016, *MNRAS*, 455, 4183
- Vogelsberger M., Marinacci F., Torrey P., Puchwein E., 2020, *Nature Reviews Physics*, 2, 42
- Walcher J., Groves B., Budavári T., Dale D., 2011, *Ap&SS*, 331, 1
- Wang E., Lilly S. J., Pezzulli G., Matthee J., 2019, *ApJ*, 877, 132
- Wang Y., et al., 2022a, *MNRAS*, 515, 3249
- Wang X., et al., 2022b, *ApJ*, 926, 70
- Weinberg D. H., 2017, *ApJ*, 851, 25
- Weinberg D. H., Andrews B. H., Freudenburg J., 2017, *ApJ*, 837, 183
- Werk J. K., et al., 2014, *ApJ*, 792, 8
- Wibking B. D., Krumholz M. R., 2022, *MNRAS*,
- Wiersma R. P. C., Schaye J., Theuns T., Dalla Vecchia C., Tornatore L., 2009, *MNRAS*, 399, 574
- Woosley S. E., Weaver T. A., 1995, *ApJS*, 101, 181
- Yabe K., et al., 2014, *MNRAS*, 437, 3647
- Yadav N., Mukherjee D., Sharma P., Nath B. B., 2017, *MNRAS*, 465, 1720
- Yates R. M., Kauffmann G., Guo Q., 2012, *MNRAS*, 422, 215
- York D. G., et al., 2000, *AJ*, 120, 1579
- Zahid H. J., Kewley L. J., Bresolin F., 2011, *ApJ*, 730, 137
- Zhao D. H., Jing Y. P., Mo H. J., Börner G., 2009, *ApJ*, 707, 354
- Zhu G., et al., 2014, *MNRAS*, 439, 3139
- Zu Y., 2020, *MNRAS*, 496, 111
- Zu Y., 2021, *MNRAS*, 506, 115
- Zu Y., Mandelbaum R., 2015, *MNRAS*, 454, 1161
- Zu Y., Mandelbaum R., 2016, *MNRAS*, 457, 4360
- Zu Y., Mandelbaum R., 2018, *MNRAS*, 476, 1637
- Zu Y., Weinberg D. H., Davé R., Fardal M., Katz N., Kereš D., Oppenheimer B. D., 2011, *MNRAS*, 412, 1059
- van den Bosch F. C., 2002, *MNRAS*, 331, 98

This paper has been typeset from a $\text{\TeX}/\text{\LaTeX}$ file prepared by the author.